Atmospheric
Measurement
Techniques

Discussions

1   **Comparison of Aircraft Measurements during GoAmazon2014/5 and**
2   **ACRIDICON-CHUVA**

3   Fan Mei[1], Jian Wang[2], Jennifer M. Comstock[1], Ralf Weigel[13], Martina Krämer[14], Christoph Mahnke[13, 8], John E.
4   Shilling[1], Johannes Schneider[8], Charles N. Long[7], Manfred Wendisch[5], Luiz A. T. Machado[3], Beat Schmid[1],
5   Trismono Krisna[5], Mikhail Pekour[1], John Hubbe[1], Andreas Giez[6], Bernadett Weinzierl[6], Martin Zoeger[6], Christiane
6   Schulz[8], Mira L. Pöhlker[8], Hans Schlager[6], Micael A. Cecchini[9], Meinrat O. Andreae[8,10], Scot T. Martin[4], Suzane, S.
7   de Sá[4], Jiwen Fan[1], Jason Tomlinson[1], Stephen Springston[2], Ulrich Pöschl[8], Paulo Artaxo[11], Christopher Pöhlker[8],
8   Thomas Klimach[8] , Andreas Minikin[12], Armin Afchine[14], Stephan Borrmann[13,8]

9   1.   Pacific Northwest National Laboratory, Richland, WA, United States.

10   2.   Brookhaven National Laboratory, Upton, NY, United States.

11   3.   National Institute for Space Research (INPE), São Paulo, Brazil

12   4.   Harvard University, Cambridge, MA, United States

13   5.   University of Leipzig, Leipzig, Germany

14   6.   Deutsches Zentrum für Luft- und Raumfahrt (DLR), Oberpfaffenhofen, Germany

15   7.   NOAA ESRL GMD/CIRES, Boulder, CO, United States

16   8.   Max Planck Institute for Chemistry, Mainz, Germany

17   9.   University of São Paulo (USP), São Paulo, Brazil

18   10. Scripps Institution of Oceanography, University of California San Diego, La Jolla, California, USA

19   11. Instituto de Física, Universidade de São Paulo, São Paulo, Brazil

20   12. DLR Oberpfaffenhofen, Flight Experiments Facility, Wessling, Germany

21   13. Institute for Physics of the Atmosphere, Johannes Gutenberg University, Mainz, Germany

22   14. Research Centre Jülich, Institute for Energy and Climate Research 7: Stratosphere (IEK-7), Jülich,
23   Germany
24

25   *Correspondence to:* Fan Mei (fan.mei@pnnl.gov)

26   **Abstract.** The indirect effect of atmospheric aerosol particles on the Earth's radiation balance
27   remains one of the most uncertain components affecting climate change throughout the industrial
28   period. This issue is partially a result of the incomplete understanding of aerosol-cloud
29   interactions. One objective of the GoAmazon2014/5 and ACRIDICON-CHUVA projects was to
30   improve the understanding of the influence of the emissions of the tropical megacity of Manaus

Atmospheric
Measurement
Techniques
Discussions

31   (Brazil) on the surrounding atmospheric environment of the rainforest and to investigate its role in

32   the life cycle of convective clouds. During one of the intensive observation periods (IOPs) in the

33   dry season from September 1 to October 10, 2014, comprehensive instrument suites collected data

34   from several ground sites. In a coordinated way, the advanced suites of sophisticated instruments

35   were deployed in situ both from the U.S. Department of Energy Gulfstream-1 (G1) aircraft and

36   the German High Altitude and Long-Range Research Aircraft (HALO) during three coordinated

37   flights on September 9, 21, and October 1. Here we report on the comparison of measurements

38   collected by the two aircraft during these three flights. Such comparisons are difficult to obtain,

39   but they are essential for assessing the data quality from the individual platforms and quantifying

40   their uncertainty sources. Similar instruments mounted on the G1 and HALO collected vertical

41   profile measurements of aerosol particles number concentration and size distribution, cloud

42   condensation nuclei concentration, ozone, and carbon monoxide concentration, cloud droplet size

43   distribution, and downward solar irradiance. We find that the above measurements from the two

44   aircraft agreed within the range given by the measurement uncertainties. Aerosol chemical

45   composition measured by instruments on HALO agreed with the corresponding G1 data collected

46   at high altitudes only. Furthermore, possible causes of discrepancies between the data sets

47   collected by the G1 and HALO instrumentation are addressed in this paper. Based on these results,

48   criteria for meaningful aircraft measurement comparisons are discussed.

49

50   1. **Introduction**

51   Dominated by biogenic sources, the Amazon basin is one of the few remaining continental

52   regions where atmospheric conditions realistically represent those of the pristine or pre-industrial

53   era (Andreae et al., 2015). As a natural atmospheric "chamber", the area around the urban region

54   of Manaus in central Amazonia is an ideal location for studying the atmosphere under natural

55   conditions as well as under conditions influenced by human activities and biomass burning events

56   (Andreae et al., 2015; Artaxo et al., 2013; Davidson et al., 2012; Keller et al., 2009; Kuhn et al.,

57   2010; Martin et al., 2016b; Pöhlker et al., 2018; Poschl et al., 2010; Salati and Vose, 1984). The

58   Observations and Modeling of the Green Ocean Amazon (GoAmazon2014/5) campaign was

59   conducted in 2014 and 2015 (Martin et al., 2017; Martin et al., 2016b). The primary objective of

60   GoAmazon2014/5 was to improve the quantitative understanding of the effects of anthropogenic

Atmospheric
Measurement
Techniques
Discussions

61   influences on atmospheric chemistry and aerosol-cloud interactions in the tropical rainforest area.

62   During the dry season in 2014, the ACRIDICON (Aerosol, Cloud, Precipitation, and Radiation

63   Interactions and Dynamics of Convective Cloud Systems)-CHUVA (Cloud Processes of the Main

64   Precipitation Systems in Brazil) campaign also took place to study tropical convective clouds and

65   precipitation over Amazonia (Wendisch et al., 2016).

66   A feature of the GoAmazon 2014/5 field campaign was the design of the ground sites'

67   location, which uses principles of Lagrangian sampling to align the sites with the Manaus pollution

68   plume (Figure 1: Source location – Manaus (T1 site), and downwind location – Manacapuru (T3

69   site)). The ground sites were overflown with the low-altitude U.S. Department of Energy (DOE)

70   Gulfstream-1 (G1) aircraft and the German High Altitude and Long Range Research Aircraft

71   (HALO). These two aircraft are among the most advanced in atmospheric research, deploying

72   suites of sophisticated and well-calibrated instruments (Schmid et al., 2014; Wendisch et al.,

73   2016). The pollution plume from Manaus was intensively sampled during the G1 and HALO

74   flights and also by the DOE Atmospheric Radiation Measurement (ARM) program Mobile

75   Aerosol Observing System and ARM Mobile Facility located at one of the downwind surface sites

76   (T3 site- 70 km west of Manaus). The routine ground measurements with coordinated and intensive

77   observations from both aircraft provided an extensive data set of multi-dimensional observations

78   in the region, which serves i) to improve the scientific understanding of the influence of the

79   emissions of the tropical megacity of Manaus (Brazil) on the surrounding atmospheric

80   environment of the rainforest and ii) to understand the life cycle of deep convective clouds and

81   study open questions related to their influence on the atmospheric energy budget and hydrological

82   cycle.

83   As more and more data sets are merged to link the ground-based measurements with

84   aircraft observations, and as more studies focus on the spatial variation and temporal evolution of

85   the atmospheric properties, it is critical to quantify the uncertainties ranges when combining the

86   data collected from the different platforms. Due to the challenges of airborne operations, especially

87   when two aircraft are involved in data collection in the same area, direct comparison studies are

88   rare. However, this type of study is critical for further combining the datasets between the ground

89   sites and aircraft. Thus, the main objectives of the study herein are to demonstrate how to achieve

90   meaningful comparisons between two moving platforms, to conduct detailed comparisons

91   between data collected by two aircraft, to identify the potential measurement issues, to quantify

92   reasonable uncertainty ranges of the extensive collection of measurements, and to evaluate the

93   measurement sensitivities to the temporal and spatial variance. The comparisons and the related

94   uncertainty estimations quantify the current measurement limits, which provide realistic

95   measurement ranges to climate models as initial conditions to evaluate their output.

96   The combined GoAmazon2014/5 and ACRIDICON-CHUVA field campaigns not only

97   provide critical measurements of aerosol and cloud properties in an under-sampled geographic

98   region but also provide a unique opportunity to understand and quantify the quality of these

99   measurements using closely orchestrated comparison flights. The comparisons between the

100   measurements from similar instruments on the two research aircraft can be used to identify

101   potential measurement issures and quantify the uncertainty range of the field measurements, which

102   include primary meteorological variables (Section 3.1), trace gases concentrations (Section 3.2),

103   aerosol particle properties (number concentration, size distribution, chemical composition, and

104   microphysical properties) (Section 3.3), cloud properties (Section 3.4), and downward solar

105   irradiance (Section 3.5). We evaluate the consistency between the measurements aboard the two

106   aircraft for a nearly full set of gas, aerosol particle, and cloud variables. Results from this

107   comparison study provide the foundation not only for assessing and interpreting the observations

108   from multiple platforms (from the ground to low altitude, and then to high altitude) but also for

109   providing high-quality data to improve the understanding of the accuracy of the measurements

110   related to the effects of human activities in Manaus on local air quality, terrestrial ecosystems in

111   rainforest, and tropical weather.

112   **2. Measurements**

113   2.1 Instruments

114   The ARM Aerial Facility deployed several in situ instruments on the G1 to measure

115   atmospheric state parameters, trace gases concentrations, aerosol particle properties, and cloud

116   characteristics (Martin et al., 2016b; Schmid et al., 2014). The instruments installed on HALO

117   covered measurements of meteorological, chemical, microphysical, and radiation parameters.

118   Details of measurements aboard HALO are discussed in the ACRIDICON-CHUVA campaign

119   overview paper (Wendisch et al., 2016). The measurements compared between the G1 and HALO

120   are listed in Table 1.

121   2.1.1 Atmospheric parameters

Atmospheric
Measurement
Techniques
Discussions

Open Access

EGU

122   All G1 and HALO meteorological sensors were routinely calibrated to maintain measurement

123   accuracy. The G1 primary meteorological data were provided at one-second time resolution based

124   on the standard developed by the Inter-Agency Working Group for Airborne Data and Telemetry

125   Systems (Webster and Freudinger, 2018). For static temperature measurement, the uncertainty

126   given by the manufacturer (Emerson) is ±0.1 K, and the uncertainty of the field data is ±0.5 K.

127   The static pressure had a measurement uncertainty of 0.5 hPa. The standard measurement

128   uncertainties were ±2 K for the chilled mirror hygrometer and 0.5 ms^{-1} for wind speed.

129   On HALO, primary meteorological data were obtained from the Basic HALO Measurement

130   and Sensor System (BAHAMAS) at one-second time resolution. The system acquired data from

131   airflow and thermodynamic sensors and from the aircraft avionics and a high-precision inertial

132   reference system to derive the basic meteorological parameters like pressure, temperature, the 3D

133   wind vector, aircraft position, and attitude. Water vapor mixing ratio and further derived humidity

134   quantities were measured by the Sophisticated Hygrometer for Atmospheric Research (SHARC)

135   based on direct absorption measurement by a tunable diode laser (TDL) system. The absolute

136   accuracy of the primary meteorological data was 0.5 K for air temperature, 0.3 hPa for air pressure,

137   0.4-0.6 ms^{-1} for wind, and 5% (±1 ppm) for water vapor mixing ratio. All sensors were routinely

138   calibrated and traceable to national standards (Giez et al., 2017; Krautstrunk and Giez, 2012).

139   2.1.2 Gas phase

140   Constrained by data availability, this comparison of trace gas measurements is focused on

141   carbon monoxide (CO) and ozone (O_3) concentrations. Those measurements were made aboard

142   the G1 by a $CO/N_2O/H_2O$ instrument (Los Gatos Integrated Cavity Output Spectroscopy

143   instrument model 907-0015-0001), and an Ozone Analyzer (Thermo Scientific, Model 49i),

144   respectively. The G1 CO analyzer was calibrated for response daily by NIST-traceable commercial

145   standards before the flight. Due to the difference between laboratory and field conditions, the

146   uncertainty of CO measurement is about ±5% for one-second sampling periods, An ultra-fast

147   carbon monoxide monitor (Aero Laser GmbH, AL5002) was deployed on HALO. The detection

148   of CO is based on a vacuum-ultraviolet-fluorimetry, employing the excitation of CO at 150 nm

149   and the precision is 2 ppb, and the accuracy is about 5%. The ozone analyzer measures ozone

150   concentration based on the absorbance of ultraviolet light at a wavelength of 254 nm. The ozone

151   analyzer (Thermo Scientific, Model 49c) in the HALO payload is very similar to the one on the

152   G1 (Model 49i), with an accuracy greater than 2 ppb or about ±5% for four-second sampling

153   periods. The G1 ozone monitor was calibrated at the New York State Department of

154   Environmental Conservation testing laboratory at Albany.

155   2.1.3 Aerosol

156   Aerosol number concentration was measured by different condensation particle counters

157   (CPCs) on the G1 (TSI, CPC 3010) and HALO (Grimm, CPC model 5.410). Although two CPCs

158   were from different manufacturers, they were designed using the same principle, which is to detect

159   particles by condensing butanol vapor on the particles to grow them to a large enough size that

160   they can be counted optically. Both CPCs were routinely calibrated in the lab and reported the data

161   at one-second time resolution. The HALO CPC operated at 0.6-1 L min^{-1}, with a nominal cutoff

162   of 4 nm. Due to inlet losses, the effective cutoff diameter increases to 9.2 nm at 1000 hPa, and

163   11.2 nm at 500 hPa (Andreae et al., 2018; Petzold et al., 2011). The G1 CPC operated at 1 L min^{-1}

164   volumetric flow rate and the nominal cut-off diameter D_{50} measured in the lab was ~10 nm.

165   During a flight, the cut-off diameter may vary due to tubing losses, which contribute less than 10

166   % uncertainty to the comparison between two CPC concentrations.

167   Two instruments deployed on the G1 measured aerosol particle size distribution. a Fast

168   Integrated Mobility Spectrometer (FIMS) inside of the G1 cabin measured the aerosol mobility

169   size from 15 to 400 nm (Kulkarni and Wang, 2006a, b; Olfert et al., 2008; Wang, 2009). The

170   ambient aerosol particles were charged after entering the FIMS inlet and then separated into

171   different trajectories in an electric field based on their electrical mobility. The spatially separated

172   particles grow into super-micrometer droplets in a condenser where supersaturation of the working

173   fluid is generated by cooling. At the exit of the condenser, a high-speed charge-coupled device

174   camera captures the image of an illuminated grown droplet at high resolution. In this study, we

175   used the FIMS 1 Hz data for comparison. The size distribution data from FIMS were smoothed.

176   Aside from the FIMS, The airborne version of the Ultra High Sensitivity Aerosol Spectrometer

177   (UHSAS) was deployed on G1 and HALO. The G1 and HALO UHSAS were manufactured by

178   the same company, and both were mounted under the wing on a pylon. UHSAS is an optical-

179   scattering, laser-based particle spectrometer system. The size resolution is around 5% of the

180   particle size. The G1 UHSAS typically covered a size range of 60 nm to 1000 nm. HALO UHSAS

181   covered 90 nm to 500 nm size range for the September 9 flight.

182 Based on operating principles, FIMS measures aerosol electrical mobility size and UHSAS

183 measures aerosol optical equivalent size. Thus, the difference in the averaged size distributions

184 from those two types of instruments might be linked to differences in their underlying operating

185 principles, such as the assumption in the optical properties of aerosol particles. The data processing

186 in the G1 UHSAS assumed that the particle refractive index is similar to ammonium sulfate (1.55),

187 which is larger than the average refractive index (1.41-0.013i) from a previous Amazon study

188 (Guyon et al., 2003). The HALO UHSAS was calibrated with polystyrene latex spheres, which

189 has a refractive index about 1.572 for the UHSAS wavelength of 1054 nm. The uncertainty due to

190 the refraction index can lead to up to 10% variation in UHSAS measured size (Kupc et al., 2018).

191 Also, the assumption of spherical particles affects the accuracy of UHSAS sizing of ambient

192 aerosols.

193 The chemical composition of submicron non-refractory (NR-PM$_1$) organic and inorganic

194 (sulfate, nitrate, ammonium) aerosol particles was measured using a high-resolution time-of-flight

195 aerosol mass spectrometer (HR-ToF-AMS) aboard the G1 (DeCarlo et al., 2006; Jayne et al., 2000;

196 Shilling et al., 2018; Shilling et al., 2013). Based on the standard deviation of observed aerosol

197 mass loadings during filter measurements, the HR-ToF-AMS detection limits for the average time

198 of thirteen seconds are approximately 0.13, 0.01, 0.02, 0.01 (3σ values) μg m^{-3} for organic, sulfate,

199 nitrate, and ammonium, respectively (DeCarlo et al., 2006). A Compact Time-of-flight Aerosol

200 Mass Spectrometer (C-ToF-AMS) was operated aboard HALO to investigate the aerosol

201 composition. Aerosol particles enter both the C-ToF-AMS and HR-ToF-AMS via constant

202 pressure inlets controlling the volumetric flow into the instrument, although the designs of the

203 inlets are somewhat different (Bahreini et al., 2008). The details about the C-ToF-AMS operation

204 and data analysis are reported in Schulz's paper (Schulz et al., 2018). The overall accuracy has

205 been reported as ~30 % for both AMS instruments (Alfarra et al., 2004; Middlebrook et al., 2012).

206 Data presented in this section were converted to the same condition as the HALO AMS data, which

207 is 995 hPa and 300 K.

208 The number concentration of cloud condensation nuclei (CCN) was measured aboard both

209 aircraft using the same type of CCN counter from Droplet Measurement Technologies (DMT,

210 model 200). This CCN counter contains two continuous-flow, thermal-gradient diffusion

211 chambers for measuring aerosols that can be activated at constant supersaturation. The

212 supersaturation is created by taking advantage of the different diffusion rates between water vapor

Atmospheric
Measurement
Techniques
Discussions

Open Access

213   and heat. After the supersaturated water vapor condenses on the CCN in the sample air, droplets

214   are formed, counted and sized by an Optical Particle Counter (OPC). The sampling frequency is

215   one second for both deployed CCN counters. Both CCN counters were calibrated using ammonium

216   sulfate aerosol particles in the diameter range of 20-200 nm. The uncertainty of the effective water

217   vapor supersaturation was ±5%. (Rose et al., 2008)

218   2.1.4 Clouds

219   Aircraft-based measurements are an essential method for in situ sampling of cloud properties

220   (Brenguier et al., 2013; Wendisch and Brenguier, 2013). Over the last 50–60 years, hot-wire probes

221   have been the most commonly used devices to estimate liquid water content (LWC) in the cloud

222   from research aircraft. Since the 1970s, the most widely used technique for cloud droplet spectra

223   measurements has been developed based on the light-scattering effect. This type of instrument

224   provides the cloud droplet size distribution as the primary measurement. By integrating the cloud

225   droplet size distribution, additional information, such as LWC can be derived from the high-order

226   data product.

227   Three cloud probes from the G1 were discussed in this manuscript. The Cloud Droplet Probe

228   (CDP) is a compact, lightweight forward-scattering cloud particle spectrometer that measures

229   cloud droplets in the 2 to 50 μm size range (Faber et al., 2018). Using a state-of-the-art electro-

230   optics and electronics, Stratton Park Engineering (SPEC Inc.) developed a Fast Cloud Droplet

231   Probe (FCDP), which also use forward-scattering to determine cloud droplet distributions and

232   concentrations in the same range as CDP with up to 100 Hz sampling rate. The G1 also carried a

233   two-dimensional stereo probe (2DS, SPEC Inc.), which has two 128-photodiode linear arrays

234   working independently and electronics produce shadowgraph images with 10 μm pixel resolution.

235   Two orthogonal laser beams cross in the middle of the sample volume, with the sample cross

236   section for each optical path of 0.8 cm^2. The manufacturer claims the maximum detection size is

237   up to 3000 μm for the 2DS. However, due to the counting statistic issue, the data used in this study

238   is from 10–1000 μm only (Lawson et al., 2006). 2DS was upgraded with modified probe tips, and

239   an arrival time algorithm was applied to the 2DS data processing. Both efforts effectively reduced

240   the number of small (shattered) particles (Lawson, 2011). For G1 cloud probes, the laboratory

241   calibrations of the sample area and droplet sizing were performed before the field deployment.

Atmospheric
Measurement
Techniques
Discussions

242   During the deployment, biweekly calibrations with glass beads were performed with the size

243   variation of less than 5%, which were consistent with the pre-campaign and after-campaign

244   calibrations. Comparison between the LWC derived from cloud droplet spectra with hot-wire

245   LWC measurement was made to estimate/eliminate the coincidence errors in cloud droplet

246   concentration measurements (Lance et al., 2010; Wendisch et al., 1996)

247   On board of HALO, two cloud probes were operated and discussed in this manuscript, each

248   consisting of a combination of two instruments: the Cloud Combination Probe (CCP) and a Cloud

249   Aerosol Precipitation Spectrometer (CAPS, denoted as NIXE-CAPS; NIXE: Novel Ice

250   Experiment). The CCP is a combination of a CDP (denoted as CCP-CDP) with a CIPgs (Cloud

251   Imaging Probe with grey scale, DMT, denoted as CCP-CIPgs). NIXE-CAPS consists of a CAS-

252   Dpol (Cloud and Aerosol Spectrometer, DMT, denoted as NIXE-CAS) and a CIPgs (denoted as

253   NIXE-CIPgs). CIPgs is an optical array probe comparable to the 2DS operated on the G1. CIPgs

254   obtains images of cloud elements using a 64-element photodiode array (15µm resolution) to

255   generate two-dimensional images with nominal detection diameter size range from 15 to 960 µm

256   (Klingebiel et al., 2015; Molleker et al., 2014).The CCP-CDP detects the forward-scattered laser

257   light by cloud particles in size range of 2.5 to 46 µm. The sample area of the CCP- CDP was

258   determined to be 0.27±0.025 mm^2 with an uncertainty of less than 10% (Klingebiel et al., 2015).

259   CAS-Dpol (or NIXE-CAS) is a light scattering probe comparable to the CDP but covers the size

260   range of 0.6 to 50 µm in diameter, thus including the upper size range of the aerosol particle size

261   spectrum (Luebke et al., 2016). Furthermore, CAS-Dpol measures the polarization state of the

262   particles (Costa et al., 2017). Correspondingly to the G1 CDP, the performance of the CCP-CDP

263   and NIXE-CAS were frequently proven by glass beads calibrations. Prior to or after each HALO

264   flight, CCP-CIPgs and NIXE-CIPgs calibrations were performed by using a mainly transparent

265   spinning disc that carries opaque spots of different but known size. The data of the CCP measured

266   particle concentration on board of HALO are corrected to gain ambient conditions using a

267   thermodynamic approach developed by (Weigel et al., 2016). For NIXE-CAPS, the size

268   distributions were provided where NIXE-CAS was merged with the NIXE-CIPgs at 20 µm.

269   2.1.5 Solar radiation

270   The G1 radiation suite included shortwave (SW, 400 - 2,700 nm) broadband total upward and

271   downward irradiance measurements using Delta-T Devices model SPN-1 radiometers. The

Atmospheric
Measurement
Techniques
Discussions

272   radiation data were corrected for aircraft tilt from the horizontal reference plane. A methodology

273   has been developed (Long; et al., 2010) for using measurements of total and diffuse shortwave

274   irradiance and corresponding aircraft navigation data (latitude, longitude, pitch, roll, heading) to

275   calculate and apply a correction for platform tilt to the broadband hemispheric downward SW

276   measurements. Additionally, whatever angular offset there may be between the actual orientation

277   of each radiometer's detector and what the navigation data say is level has also been determined

278   for the most accurate tilt correction.

279   The Spectral Modular Airborne Radiation measurement sysTem (SMART-Albedometer) was

280   installed aboard HALO. Depending on the scientific objective and the configuration, the optical

281   inlets determining the measured radiative quantities can be chosen. The SMART-Albedometer has

282   been utilized to measure the spectral upward and downward irradiances; thereby it is called as an

283   albedometer, as well as to measure the spectral upward radiance. The SMART-Albedometer is

284   designed initially to cover measurements in the solar spectral range between 300 and 2,200 nm

285   (Krisna et al., 2018; Wendisch et al., 2001; Wendisch et al., 2016). However, due to decreasing

286   sensitivity of the spectrometers at large wavelengths, the use of the wavelengths was restricted to

287   300 – 1,800 nm. The spectral resolution is defined by the full width at half maximum (FWHM),

288   which is between 2 and 10 nm. In this case, the instruments were mounted on an active horizontal

289   stabilization system for keeping the horizontal position of the optical inlets during aircraft

290   movements (up to +/- 6 degrees from the horizontal plane).

291   2.2 Flight patterns

292   During the dry season IOP (September 1 – October 10, 2014), two types of coordinated flights

293   were carried out: one flight in cloud-free condition (September 9) and two flights with clouds

294   present (September 21 and October 1). In this study, we compare the measurements for both

295   coordinated flight patterns. The discussion is mainly focused on the flights under cloud-free

296   conditions on September 9 and the flight with clouds present on September 21, as shown in figure

297   1. The other coordinated flight on October 1 is included in the supplemental document.

298   For the cloud-free coordinated flight, the G1 took off first and orbited around an area from the

299   planned rendezvous point until HALO arrived in sight. It then coordinated with HALO and

300   performed a wing-to-wing maneuver along straight legs around 500 m above sea level, as shown

301   in Figure 2. The normal G1 average sampling speed is 100 m s^{-1}, and the normal HALO average

Atmospheric
Measurement
Techniques
Discussions

Open Access

302   sampling speed is 200 m s^{-1}. During the coordinated flight on September 9, both aircraft also

303   adjusted their normal sampling speed by about 50 m s^{-1} so that they could fly side by side.

304   For the second type of coordinated flights, the G1 and HALO flew the stacked paten at their

305   own normal airspeed. On September 21, the G1 also took off from the airport first, followed by

306   HALO 15 minutes later. Then, both aircraft flew above the T3 ground site and subsequently flew

307   several flight legs stacked at different altitudes. The two aircraft were vertically separated by about

308   330 m and sampled below, inside, and above clouds. Due to the different aircraft speeds, the flight

309   distance between two aircraft flight paths continued increasing from 15 min to 1 hour, as shown

310   in Figure 3. On October 1, the G1 focused on the cloud microphysical properties and contrasting

311   polluted versus clean clouds. HALO devoted the flight to the cloud vertical evolution and life cycle

312   and also probed the cloud processing of aerosol particles and trace gases. The G1 and HALO

313   coordinated two flight legs between 950–1250 m above the T3 site under cloud-free conditions.

314   Following that, HALO flew to the south of Amazonia, and the G1 continued sampling plume-

315   influenced clouds above the T3 site, and then flew above the Rio Negro area.

316   In this study, to perform a meaningful comparison of in situ measurements, all the data from

317   instruments were time synchronized with the aircraft (G1 or HALO) navigation system. For AMS

318   and CPC data, the time shifting due to tubing length and instrument flow had been corrected. For

319   the coordinated flight on Sep. 9, the data compared was from the same type of measurements with

320   the same sampling rate. For the measurements with the different sampling rate, the data were

321   binned to the same time interval for comparison. For the flight with the cloud presents (Sep.21 and

322   Oct. 1), the following criteria are used: 1) the data collected by the two aircraft must be less than

323   30 mins apart from each other; 2) the comparison data was binned to 200 m altitude interval; and

324   3) the cloud flag was applied to the aerosol measurements, and the data affected by the cloud

325   shattering are eliminated from the comparisons of aerosol measurements. Moreover, additional

326   comparison criteria are specified for individual measurements in the following section. Tables 2

327   shows the total number of points used for the comparison.

328   **3. Results**

329   3.1 Comparison of the G1 and HALO measurements of atmospheric state parameters

330   The atmospheric state parameters comprise primary variables observed by the research aircraft.

331   The measurements provide essential meteorological information not only for understanding the

Atmospheric
Measurement
Techniques
Discussions

332   atmospheric conditions but also for providing the sampling conditions for other measurements,

333   such as those of aerosol particles, trace gases, and cloud microphysical properties.

334   For cloud-free coordinated flights, the comparison focused on the near side-by-side flight leg

335   at around 500 m, as shown in Figure 2. Table 3 shows the basic statistics of the data for primary

336   atmospheric state parameters. In general, the atmospheric state parameters observed from both

337   aircraft were in excellent agreement. The linear regression achieved a slope was near 1 for four

338   individual measurements. The regression is evaluated using the below equation 1.

339    $$R^2 = 1 - \frac{SS_{regression}}{SS_{Total}} \qquad (1)$$

340   Where the sum squared regression error is calculated by $SS_{regression} = \sum(y_i - y_{regression})^2$,

341   and the sum squared total error is calculated by $SS_{Total} = \sum(y_i - \bar{y})^2$, y_i is the individual data

342   point, $\bar{y}$ is the mean value, and $y_{regression}$ is the regression value. When the majority of the data

343   points are in a narrow value range, using the mean is better than the regression line and the R^2 will

344   be negative (Neg in Table 3).

345   The difference between the average ambient temperatures on the two aircraft was 0.5 K, and

346   the difference between the average dew point temperatures was about 1 K. For temperature and

347   humidity, the G1 data were slightly higher than the HALO data. The main contributions to the

348   observed differences include the error propagation in the derivation of the ambient temperature

349   from the measured temperature, instrumental-measurement uncertainty, and the temporal and

350   spatial variability. The average horizontal wind speed measured by HALO is 0.4 m s^{-1} higher than

351   the average horizontal wind speed measured by the G1. The uncertainty source of wind estimation

352   is mainly due to the error propagation from the indicated aircraft speed measurement and the

353   aircraft ground speed estimation from GPS. The static pressure distribution measured aboard

354   HALO showed a smaller standard deviation (0.9 hPa) compared to the value of the G1 (1.5 hPa).

355   The standard deviation (std) was also 0.6 hPa narrower. Part of the reason for this difference is a

356   more substantial variation of the G1 altitude during level flight legs when G1 flew at around 50

357   m/s higher than its normal airspeed. Thus, any biases caused by their near side-by-side airspeeds

358   being different from their normal airspeeds would be undetected during these coordinated flights.

359   For the coordinated flights under cloudy conditions, we used the criteria from Section 2 to

360   compare ambient conditions measured by the G1 and HALO aircraft. As shown in Figure 4, the

361   linear regression slopes for ambient temperature, dew point temperature, and pressure were also

362   close to 1 between the G1 and HALO measurements during the September 21 coordinated flight.

363   The R^2 value is also close to 1. These results suggest that the G1 and HALO measurements

364   achieved excellent agreements. The dew point temperature from the G1 measurement was

365   erroneous between 2200–2700 m and above 3700 m (Figure 4(c)) because the G1 sensor was

366   skewed by wetting in the cloud. The HALO dew point temperature was calculated from the total

367   water mixing ratio measured by TDL, and that measurement in the cloud was more accurate than

368   the measurement made by the chilled mirror hydrometer aboard the G1.

369   The lower value of the R^2 value in horizontal wind speed means the ratio of the regression error

370   and total error in wind measurement is much higher than the temperature and pressure

371   measurements. The main contributions to this difference are the error propagation during the

372   horizontal wind speed estimation and also the temporal and spatial variance between two aircraft

373   sampling location. We observed differences between the two aircraft data of up to 2 m s^{-1}, caused

374   by the increasing sampling distance as the two aircraft were climbing up. For example, the G1

375   flew a level leg above T3 around 2500 m between 16:20-16:30, while HALO stayed around 2500

376   m for a short period and kept climbing to a higher altitude. Due to strong vertical motion,

377   turbulence, and different saturations (evaporation-condensation processes), the variances in the

378   horizontal wind speed (Figure 4(d)) were also more significant compared to the variances of

379   temperature and pressure measurements.

380   3.2 Comparison of trace gas measurements

381   For the cloud-free coordinated flight, ozone is the only trace gas measurement available on both

382   aircraft. The linear regression slope shows that the HALO ozone concentration was about 8%

383   higher than the G1 concentration. The difference between the averaged ozone concentrations was

384   4.1 ppb. The primary source of bias is probably the different ozone loss in the sampling and transfer

385   lines.

386

387   The comparison made on September 21 flight in Figure 5 shows good agreement for the

388   vertically averaged ozone measurements. Comparing the statistics data from September 9, the

389   ozone measurement is not sensitive to the temporal and spatial changes. The G1 CO measurement

390   shows a low R^2 value which is mainly from the systematic bias between the two instruments with

391   different operation principles. The larger variance between 2000-3000 m in CO concentration

Atmospheric
Measurement
Techniques
Discussions
Open Access
EGU

392   indicates the spatial variation contribution, while the G1 and HALO were sampling different air

393   masses, as indicated in Figure S7.

3.3 Comparison of aerosol measurements

395   Aerosol particles exhibited strong spatial variations, both vertically and horizontally, due to

396   complex atmospheric processing in the Amazon basin, especially with the local anthropogenic

397   sources at Manaus. Thus, any spatially resolved measurement is critical to characterizing the

398   properties of the Amazonian aerosols. The cloud-free coordinated flights provide us with suitable

399   data to compare the G1 and HALO aerosol measurements and thus will enable further studies

400   combined with the ground measurements. The vertical profiles obtained using the G1 and HALO

401   platforms in different aerosol regimes in the Amazon basin have contributed to many studies (Fan

402   et al., 2018; Martin et al., 2017; Wang et al., 2016).

403   When comparing the measurements from the two aircraft, the inlet system is a critical item,

404   especially for sampling aerosol particles (Wendisch et al., 2004). Inlet design and characterization

405   can actively modify the measured aerosol particle number concentration, size distribution, and

406   chemical composition. The G1 aerosol inlet is a fully automated isokinetic inlet. Based on the

407   manufacturer wind tunnel test and peer-reviewed publications, this inlet operates for aerosol up to

408   5 μm, with transmission efficiency around 50 % at 1.5 μm (Dolgos and Martins, 2014; Kleinman

409   et al., 2007; Zaveri et al., 2010). The HALO sub-micrometer Aerosol Inlet (HASI) was explicitly

410   designed for HALO. Based on the numerical flow modeling, optical particle counter

411   measurements, and field study evaluation, HASI has a cut-off size of 3 μm, with transmission

412   efficiency larger than 90 % at 1 μm (Andreae et al., 2018; Minikin et al., 2017).

3.3.1   Aerosol particle number concentration

414   For the cloud-free coordinated flight, the linear regression of CPC and UHSAS between the G1

415   and HALO measurements are also included in Table 3. Also, the total number concentration of

416   HALO CPC data was about 20 % lower than the total number concentration from the G1 CPC, as

417   shown in Figure 6. The typical uncertainty between two CPCs is 5-10%.(Gunthe et al., 2009; Liu

418   and Pui, 1974) Many factors can contribute to the rest 10-15% difference. Those include

419   systematic uncertainties, such as systematic instrument drifts, different aerosol particle losses

420   inside of the two CPCs, and different inlet transmission efficiencies in the two aircraft.

421   The CPC data in Figure 6 are color-coded with UTC time. The general trend is that the aerosol

422   number concentration increased with aircraft sampling through the Manaus plume between 15:30-

423   15:40. A similar trend was observed in aerosol particle number concentration (Figure 7) measured

424   by the Ultra-High Sensitivity Aerosol Spectrometer (UHSAS)-Airborne version (referred to as

425   UHSAS). The total number concentration data given by UHSAS (Figure 7) is integrated over the

426   overlapping size range (90 – 500 nm for the September 9 flight) for both the G1 and HALO

427   UHSAS. The linear regression shows that the total aerosol particle concentration from HALO

428   UHSAS is about 16.5% higher than the total aerosol concentration from the G1 UHSAS. The

429   discrepancy between the two UHSAS measurements is mainly due to the error propagation in the

430   sampling flow, the differential pressure transducer reading, the instrument stability, and calibration

431   repeatability, which is consistent with the other UHSAS study (Kupc et al., 2018). In the airborne

432   version of UHSAS, mechanical vibrations have a more significant impact on the pressure

433   transducer reading than the case for the bench version of UHSAS.

434   For the coordinated flight on September 21, the G1 and HALO data are averaged to a 200 m

435   vertical altitude interval, as shown in Figure 8. There was a good agreement in the CPC

436   comparison, especially at altitudes of 200 m and above (<10 % variance). However, the linear

437   regression slope significantly decreased, which was primarily related to the temporal and spatial

438   differences in aerosol number concentration. Especially between 2000 – 3000 m altitude, the

439   difference between the G1 and HALO measurement is largely due to the different aerosol srouces,

440   as shown in Figure S6(a). The size range was integrated from 100–700 nm for UHSAS on

441   September 21. The change of the size range was because the overlap of size distribution from both

442   UHSAS instruments was changed. The linear regression slope and the R^2 value slightly decreased

443   in the UHSAS comparison as shown in Figure 8(b). And we can expect that the main contribution

444   to the UHSAS measurement difference is from instrument systematic drift and the spatial/temporal

445   variance of particle concentration in the ambient environment as shown in Figure S6(b). However,

446   combining with the CPC measurement comparison, it indicates that the smaller size aerosol

447   particles (< 100 nm) have a more profound variance due to the temporal and spatial change.

448   3.3.2   Aerosol particle size distribution

449   For the cloud-free coordinated flight, the averaged aerosol size distribution measured during

450   one flight leg is compared in Figure 9. Based on the comparison plot, at the size range less than 90

451   nm, the G1 UHSAS overestimated the particle counts, which is due to the error in the counting

452   efficiency correction. The UHSAS detection efficiency is close to 100% for particles larger than

453   100 nm and concentrations below 3000 cm^{-3} but decreases both for smaller particles and for higher

454   concentrations considerably (Cai et al., 2008). The aerosol counting efficiency correction

455   determined from the lab condition does not represent the real correction during the flight operation.

456   Between 90 nm and 250 nm, FIMS agreed well with the G1 UHSAS, whereas HALO UHSAS is

457   about 30 % higher than the other two instruments. For the size range of 250–500 nm, FIMS had

458   good agreement with HALO UHSAS, whereas FIMS is about 30-50 % higher than the G1 UHSAS

459   depending on the particle size. Because the UHSAS has a simplified "passive" inlet, the large size

460   aerosol particle loss in the UHSAS inlet was expected to increase with the increase of the aircraft

461   speed. Thus, the lower G1 UHSAS counts at a larger aerosol particle size are likely related to the

462   particle loss correction.

463   For the September 21 flight, the aerosol size distribution vertical profiles were averaged into

464   100 m altitude intervals (Figure 10). Overall, all size distribution measurements captured the mode

465   near 100 nm between 800–1000 m, which is at the top of the convective boundary layer, as

466   indicated by the potential temperature (Figure 10(d)), which starts from a maximum near the

467   ground and then becomes remarkably uniform across the convective boundary layer. With the

468   increase in altitude, we observe the peak of the aerosol size distribution shifted from 100 nm to

469   150 nm. Note that due to data availability, the aerosol size distribution data from the HALO

470   UHSAS has a less spatial resolution.

471   3.3.3   A significant contribution of small aerosol particles

472   Comprehensive characterization of aerosol particles, especially small ones (<50 nm)

473   during GoAmazon2014/5 has demonstrated that high concentrations of those small particles in the

474   lower free troposphere are transported from the free troposphere into the boundary layer by a

475   strong convective downdraft and sustain the population of particles in the pristine Amazon

476   boundary layer. This important observation improved the current understanding of the aerosol

477   influence on cloud properties and climate under natural conditions (Fan et al., 2018; Wang et al.,

478   2016). However, the aerosol particle size distribution measurement, especially for sizes less than

479   50 nm, is very rare due to the lack of high-frequency airborne measurements. The most common

480   aerosol size spectrometer, UHSAS, covers aerosol particle sizes larger than 60 nm. The scanning

Atmospheric
Measurement
Techniques
Discussions

481   mobility particle spectrometer cannot obtain size distribution in 1 Hz time resolution. The other

482   approach is to estimate particle size distribution by extrapolating the UHSAS or Passive Cavity

483   Aerosol Spectrometer Probe (size range 100 – 3000 nm) measured aerosol size distribution to

484   smaller size ranges (down to 10 nm). The accuracy of the third approach is limited by the nature

485   of the aerosol size distribution, and the aerosol particle concentration can be significantly

486   underestimated if there is a dominant nucleation mode in the aerosol particle size distribution, such

487   as during a new particle formation event.

488   As shown in Figure 11, we compared the integrated aerosol number concentrations

489   between one wet season flight (on March 7), which was influenced by a long-range transport plume

490   from Africa (Moran-Zuloaga et al., 2018) and one typical dry season flight (September 21). The

491   agreement of the small aerosol number concentration between the FIMS-measured size

492   distribution and UHSAS/PCASP estimated size distribution is reasonably good for the dry season

493   flight when the accumulation mode dominated the aerosol particle size distribution. During the

494   wet season, there was a strong vertical gradient in the particle size spectrum above central

495   Amazonia under clean conditions. Thus, we can observe an increase of underestimation of the

496   small size particle concentration both for the size ranges less than 50 nm and less than 100 nm, as

497   the filled markers move away from each other with the increase of altitude. Because of the

498   negligible mass contribution to the total aerosol loading, those ultrafine aerosol particles (< 50 nm)

499   are conventionally considered too small to affect cloud formation. However, the new observational

500   evidence and numerical simulation of deep convective clouds outlined a new mechanism, which

501   suggests an energetic anthropogenic invigoration of deep convective clouds by those ultrafine

502   aerosol particles in previously pristine regions of the world (Fan et al., 2018). Two newly published

503   studies (Fan et al., 2018; Wang et al., 2016) emphasize the importance of the airborne observation

504   and suggest the ultrafine aerosol particles (<50 nm) measurement should be included as a baseline

505   routine measurement in future airborne experiments.

506   For field studies without the deployment of FIMS, one option to assess the accuracy of

507   UHSAS/PCASP estimated size distribution is to compare the total number concentration based on

508   the integration of the UHSAS/PCASP estimated size distribution to the total number concentration

509   from CPC. For field study focusing on the high concentration and variability of sub-50 or sub-100

510   nm aerosol particles, such as new particle formation events, it is highly recommended to request

Atmospheric
Measurement
Techniques
Discussions

the deployment of FIMS. Due to the limited availability of FIMS, one option is to use several well-characterized CPCs, which operate at the different cut-off sizes, to measure the ambient aerosol simultaneously, and then use the data-inversion technique to estimate the aerosol size distribution of sub-50 or sub-100 nm aerosol particles. Another reasonable substitute to the FIMS might be a Scanning Mobile Particle Sizer (SMPS), but it should be noted that on an airborne platform an SMPS does not nearly have the same time resolution as a FIMS. To better adapt the spatial change in aerosol concentration, a residence chamber similar to a system described in another study (Kotchenruther and Hobbs, 1998) should be deployed with SMPS.

3.3.4 Aerosol particle chemical composition

Figure 12(a) shows vertical profiles of the total mass concentrations measured by the two AMS instruments on September 21. Above 2500 m altitude, the agreement between the two instruments is excellent (mean difference less than 5%). Between 2000 and 2500 m, the agreement is within the uncertainty range. Below 2000 m altitude, however, the aerosol particle mass concentrations measured by the AMS operated on HALO are lower than the concentrations measured by the AMS on the G1. The aerosol volume concentrations from G1 AMS was converted from the mass concentration from AMS, by assuming the organic compound density was 1.5 g cm-3 (Pöschl et al., 2010). The converted aerosol volume concentration agreed well with the volume concentration calculated based on UHSAS data below 2500 m, as shown in Figure 12(b). The agreement at lower altitudes suggests that the lower concentration in HALO AMS is due to the transmission efficiency issue in the constant pressure inlet used by HALO AMS. This inlet was a prototype, designed and built at MPIC Mainz, and works by changing the size of the critical orifice that regulates the flow into the aerodynamic lens. The design and transmission characteristics will be described in an upcoming publication (Molleker, S., in prep.). The AMS aboard the G-1 used a constant pressure inlet based on the design in Bahreini et al., 2008. Thus, we conclude that data above 2500 m altitude measured by the AMS aboard HALO in 2014 are valid, while data below 2500 m need to be corrected using correction factors derived from laboratory characterization before further study. After 2014, the HALO inlet design was improved to address the inlet transmission issues specific to this field campaign.

3.3.5 CCN number concentration

Atmospheric
Measurement
Techniques
Discussions

540   These measurements provide valuable information about the aerosol's ability to form cloud

541   droplets and modify the microphysical properties of clouds. Numerous laboratory and field studies

542   have improved the current understanding of the connections between aerosol particle size,

543   chemical composition, mixing states and CCN activation properties (Bhattu and Tripathi, 2015;

544   Broekhuizen et al., 2006b; Chang et al., 2010; Duplissy et al., 2008; Lambe et al., 2011; Mei et al.,

545   2013a; Mei et al., 2013b; Pöhlker et al., 2016; Thalman et al., 2017). In addition, based on the

546   simplified chemical composition and internal mixing state assumption, various CCN closure

547   studies have achieved success within ±20% uncertainty for ambient aerosols (Broekhuizen et al.,

548   2006a; Mei et al., 2013b; Rissler et al., 2004; Wang et al., 2008).

549   According to earlier studies (Gunthe et al., 2009; Pöhlker et al., 2016; Roberts et al., 2001;

550   Roberts et al., 2002; Thalman et al., 2017), the hygroscopicity (κ_{CCN}) of CCN in the Amazon basin

551   is usually dominated by organic components (κ_{Org}). Long-term ground-based measurements at the

552   Amazon Tall Tower Observatory also suggested that there were low temporal variability and no

553   pronounced diurnal cycles in hygroscopicity only under natural rainforest background conditions

554   (Pöhlker et al., 2018; Pöhlker et al., 2016).

555   Using FIMS and CCN data from both the G1 and HALO collected during the coordinated flight

556   leg on September 9, the critical dry diameter (D_{50}) was determined by integrating FIMS size

557   distribution to match the CCN total number concentration. Then, D_{50} was combined with the CCN-

558   operated supersaturation to derive the effective particle hygroscopicity by applying the k-Köhler

559   theory. The histogram plots based on the density of the estimated hygroscopicity (κ_{est}) from both

560   aircraft were compared for the flight leg above T3. For the G1 and HALO data, the κ_{est} value

561   derived from the flight leg above the T3 site is 0.186±0.067 and 0.189±0.083 separately. That

562   value is also slightly higher than the overall mean kappa derived from long-term measurements

563   from the Amazon Tall Tower Observatory, which is 0.17±0.06 (Pöhlker et al., 2016; Thalman et

564   al., 2017).

565   An example of a comparison of vertical profiles of the CCN concentration at 0.5%

566   supersaturation on September 21 is shown in Figure 13. The difference between CCN

567   measurements on the two aircraft is about 20% on average. However, the linear regression slope

568   increases to 0.9120 if we focused on the data above 2500 m. The main contributions to the

569   difference include the difference in aerosol inlet structure, aerosol particle loss correction in the

570   main aircraft inlet and the constant pressure inlet, the systematic inlet difference below 2500 m as

571   shown in AMS data, and the error propagation of CCN measurements.

572   3.4 Comparison of cloud measurements

573   In situ cloud measurements help to capture the diversity of different cloud forms and their

574   natural temporal and spatial variability. The G1 CDP and FCDP were deployed under the different

575   wing pylons, and also on the different side of the aircraft. The G1 2DS was deployed on the same

576   side of FCDP. The HALO cloud combination probe (CCP-CDP and CCP-CIPgs) and NIXE-CAPS

577   (NIXE-CAS and NIXE-CIPgs) were deployed under the different wing pylons but on the same

578   side of the aircraft. On September 21, 2014, based on the aircraft location and elevation

579   information as shown in Figure 1(b) and Figure 3, two aircraft were sampling above T3 site and

580   passing through the same cloud field at ~1600 m flight leg and ~1900 m flight leg as shown in

581   Figure S8 and Figure S9. We used the cloud probes data from ~1900 m flight leg for the cloud

582   droplet number concentration comparison. Two size ranges were considered: 3-20 μm from light

583   scattering probes (CDP vs. FCDP on the G1, CCP-CDP vs. NIXE-CAS on HALO) and 2-960 μm

584   from combined cloud probes.

585   3.4.1   Comparison of cloud droplet number concentration between 3-20 μm

586   The primary cloud layer was observed by both the G1 and HALO between 1000-2500 m above

587   ground. Although the two aircraft have sampled along the same flight path, the instruments

588   probably observed different sets of the cloud due to cloud movement with the prevailing wind or

589   different cloud evolution stages. Thus, an initial comparison focuses on the redundant instruments

590   on the same aircraft, that measured truly collocated and synchronous on board of HALO and of

591   the G1, respectively. In Figure 14 (a), the data of the CCP-CDP and of the NIXE-CAS are

592   juxtaposed sampled over about 13 minutes for particles detection size ranges which were

593   considered as most equivalent. The comparison reveals two ranges of particle number

594   concentrations at which densification of agreeing measurements become visible. At very low

595   number concentrations (about 10^{-1} – 10 per cm³) the presence of inactivated (interstitial) aerosols

596   in the clear air space between the very few cloud elements should be considered. Over specific

597   ranges, however, the fine structure of varying cloud droplet number concentration may cause the

Atmospheric
Measurement
Techniques
Discussions

598   regression's scattering, indicated by cloud particle measured by one instrument whilst respective

599   antagonist seems to measure within almost clear air – and vice versa. At higher number

600   concentrations, i.e., between 10^2 and 10^3 per cm³, the comparison of the highly resolved data

601   constitutes increasing compactness with respect to the 1:1 line. The overall data scatter of this

602   comparison, however, may indicate the highly variable structure within clouds as those

603   investigated over the Amazon basin. The data of the G1 CDP and the FCDP are juxtaposed as the

604   same as HALO cloud probes. However, the sampled cloud period was much shorter – about 3

605   minutes. Similar as the HALO cloud probes comparison, we observe two ranges of particle number

606   concentrations at which a densification of agreeing measurements become visible, especially for

607   the lower number concentrations, in Figure 14(b). At higher number concentrations, only a few

608   cloud elements were observed by the G1 cloud probes. That is because the G1 was about 7-23

609   minutes later to pass the same location as HALO, and experienced much fewer cloud elements.

610   3.4.2   Comparison of cloud droplet size distribution between 2-960 µm from both aircraft

611   Comparing the cloud probes from the G1 and HALO, although it seems that the size

612   distributions never match better than for the cloud particle diameter size range below 10 µm, the

613   size distributions from two aircraft are in remarkably good agreement, considering the instance

614   that the cloud detection on board the G1 occurred 7-23 minutes after the cloud probing on board

615   of HALO, as shown in Figure 15. On HALO, the CCP and NIXE-CAPS probes agreed very well

616   between 2-960 µm and both peaked around 10 µm. On the G1, although CDP and FCDP has a

617   more significant difference in the size range less than 8 µm, both of them showed the peak of the

618   size distribution was around 15 µm. The difference between the G1 CDP and FCDP may be due

619   to the data post-processing. Additional coincidence correction and shattering correction were

620   applied to FCDP, but not to CDP. For cloud elements larger than 10 µm, the difference between

621   the obtained cloud particle size distributions from two aircraft becomes substantial (up to two

622   orders of magnitude) which may be indicative for observations of two different stages within the

623   progressing development of a precipitation cloud which is particularly expressed in elevated

624   number concentrations of larger cloud elements observed during the G1 measurement that

625   happened later. We also observed that the general cloud characteristic is similar at different altitude

626   levels as shown in Figure S10. The first two of three averaged periods were chosen during the

627   flight leg of ~1600 m and the last average period is for the flight leg ~1900 m compared in Figure

Atmospheric
Measurement
Techniques
Discussions

628   15. Due to the averaging, the fine in-cloud structure gets suppressed. The small scale variabilities

629   inside a cloud which are illustrated by the scattering of the highly resolved measurement data from

630   the instrument comparison (cf. Figure 14) and the temporal evolution of in-cloud microphysics are

631   not ascertainable and furthermore are beyond the scope of this study.

632   3.5 Comparison of radiation measurements

633   In this study, the downward irradiance measured by the SPN-1 unshaded center detector

634   was compared with the integrated downward irradiance from the SMART-Albedometer between

635   300–1,800 nm wavelengths in Figure 16. Only measurements from flight legs, where the G1 and

636   HALO flew near side-by-side and at the same altitude were taken into consideration for analysis.

637   In Figure 16, the top panel shows the time series of SPN-1 measurements, and the bottom panel

638   shows the time series of SMART-Albedometer measurements. The black dots represented all data,

639   and the blue circles identified data when the navigation condition was within +/- 1 degree from the

640   horizontal level. The large scatter in the data between 15:12-15:28 and 15:35-15:40 is mainly due

641   to the different sensor trajectories during the maneuvering of the aircraft to get to the coordinated

642   flight position. Because of the difference of each aircraft position from horizontal, the measured

643   signal varied from the signal of the direct component of sunlight. Each sensor might look at

644   different directions of the sky or different parts of the clouds. In addition, both aircraft flew under

645   scattered clouds, and this uneven sunlight blocking is another contribution to the "drop-off"

646   behavior in the time series plots of the downward irradiance.

647   Comparing the G1 and HALO measurements between 15:15-1:55 using the restricted

648   navigation criteria in Figure 17, we observed that the G1 SPN1 irradiance is slightly higher than

649   the integrated irradiance from the SMART-Albedometer. However, the difference in the averaged

650   irradiance is less than 10 %. That result could be due to the difference in radiometer spectral ranges:

651   400–2700 nm (SPN1 radiometer) vs. 300–1800 nm (SMART).

652   **4   Uncertainty assessment**

653   As mentioned in the introduction, a low-flying G1 and a high-flying HALO cover the sampling

654   area from the atmospheric boundary layer, low clouds to the free troposphere, and the sampling

655   period from the dry and wet seasons (Martin et al., 2016a). This spatial coverage provides the user

656   community with abundant atmospheric-related data sets for their further studies, such as for remote

Atmospheric
Measurement
Techniques
Discussions

657   sensing validation and modeling evaluation. However, one critical step to bridge the proper usage

658   of the observation with further atmospheric science study is to understand the measurement

659   uncertainty in this data set, especially the variation between the coexisting measurements due to

660   the temporal and spatial difference.

661   For the major measurements during this field study, three primary sources contribute to the

662   measurement variation between the two aircraft: the temporal and spatial variations, the difference

663   in the inlet characterization, and the limitation of the instrument capability. The difference in the

664   inlet characterization and the instrument error are the same between the coordinated flights on

665   September 9 and September 21. Thus, we can examine the sensitivity of each measurement to the

666   spatial variation by comparing two flights. For the majority of the comparisons of the September

667   21 flight, there are no significant spatial and temporal variation between two aircraft

668   measurements. However, we noticed the comparison uncertainty is more significant between 2000

669   – 3000 m altitude than the other altitudes in the aerosol and trace gas profile, especially for the

670   aerosol particles smaller than 100 nm. This additional difference occurring between 2000-3000 m

671   indicates the spatial variation contribution, while the G1 and HALO were sampling different air

672   masses. The G1 had one flight leg around 2500 m above T3 site, while HALO continued climbing

673   through 2000-3000 m range to reach the next flight leg around 4500 m. Thus, for the G1

674   measurements, the data show two modes in the histogram distribution. The large mode was

675   typically from the data when the G1 passed through the pollution plume, and the small mode

676   represented the background value. Because the flight path of HALO did not pass through the

677   plume, their data shows only one mode in the histogram plots, as shown in S6 and S7 in the

678   supplemental material.

679   For atmospheric meteorological variables, the overall uncertainty is relatively smaller (less

680   than 1 %) comparing to the other airborne measurements. The main contribution for the three-

681   dimensional wind measurement is more sensitive to the spatial variation than the ambient

682   temperature and pressure due to the complex turbulence structure in the boundary layer (see Figure

683   S5). The other measurement affected mainly by the spatial and temporal variation is the cloud

684   measurements, which is consistent with a previous study (Andreae et al., 2004). The considerable

685   variation in the comparison between 2-960 μm indicates the evolution of cloud droplet size

686 distributions (DSDs) over time and space has a more significant influence on the large droplet size,

687 and it serves as the major contributor for the DSDs comparison.

688 The inlet also significantly affects the aerosol and gas phase measurements. Inlet

689 characterizations are inherently challenging. However, comparisons as shown here can be used to

690 assess the performance of the inlets indirectly. In this study, reasonable agreement of the total

691 number concentration of aerosol particles between two CPCs indicated the uncertainty caused by

692 the main aerosol inlet difference is less than 15%. In addition to the main aerosol inlet, the particle

693 losses caused by AMS aerosol constant pressure inlet also affects the AMS comparison below

694 2500 m altitude. Based on a literature survey, this study, for the first time, compares the non-

695 refractory particle mass concentration between two aircraft measurements. Although two AMS

696 sampled different air masses during the majority of the campaign, the excellent agreement between

697 the two measurements from the comparison flight linked the aerosol chemical composition from

698 the wet to dry season and from the atmospheric boundary layer to the upper troposphere.

699 We also noticed that the CCN and UHSAS comparisons are associated with more substantial

700 uncertainties because of the more complex instrument designs. The aerosol flow fluctuation, the

701 CCN column temperature fluctuation, and the stabilization of the optical particle counter all

702 contribute to the accurate estimation of the CCN concentration. In a similar sense, the aerosol flow

703 fluctuation, the difference in the inlet efficiency at different platform speeds, the laser temperature

704 fluctuation, and the signal-to-noise ratio at lower size range all contribute to the considerable

705 uncertainty of the UHSAS concentration measurement. However, the CCN hygroscopicity

706 estimation on the near side-by-side comparison on September 9, 2014, shows very encouraging

707 agreement. Thus, the spatial variance and the instability of the CCN and UHSAS performance

708 both led to the variance between two aircraft of up to 50% based on the comparison scenario on

709 September 21, 2014. This remains the most significant variance we observed during these two

710 aircraft measurement comparisons.

711 The summary of the major measurement uncertainty contributed by the spatial difference

712 between the two aircraft is listed in Table 4.

713

Atmospheric
Measurement
Techniques
Discussions

5 Summary

In situ measurements made by well-characterized instruments installed on two research aircraft (the G1 and HALO) during the GoAmazon 2014/5 and ACRIDICON-CHUVA campaigns were compared. Overall, the analysis shows good agreement between the G1 and HALO measurements for a relatively broad range of atmospheric-related variables in a challenging strophic environment. Measured variables included atmospheric state parameters, aerosol particles, trace gases, clouds, and radiation properties. This study outlines the well-designed coordinated flights for achieving a meaningful comparison between two moving platforms. The high data quality was ensured by the most sophisticated instruments aboard two aircraft used the most advanced techniques, assisted with the best-calibrated/characterized procedures. The comparisons and the related uncertainty estimations quantify the current measurement limits, which provide the guidance to the modeler to realistically quantify the modeling input value and evaluate the variation between the measurement and the model output. The comparison also identified the measurement issues, outlined the associated reasonable measurement ranges, and evaluated the measurement sensitivities to the temporal and spatial variance.

The comparisons presented here were mainly from two coordinated flights. The flight on September 9 was classified as a cloud-free flight. During this flight, the G1 and HALO flew near side-by-side within a "polluted" leg, which was above the T3 site and across the downwind pollution plume from Manaus, and a "background" leg, which was outbound from Manaus to the west and could be influenced by the regional biomass burning events during the dry season. Both legs were at 500 m altitude and showed linear regression slopes of ambient temperature and pressure, horizontal wind speed and dew point temperature near to 1 between the G1 and HALO measurements. These comparisons provide a solid foundation for further evaluation of aerosol, trace gas, cloud, and radiation properties. The total aerosol concentration from CPC and UHSAS were compared for the 500 m flight leg above the T3 site. The UHSAS measurement had a better agreement than the CPC measurement. That is because of the minor difference in the inlet structure and instrument design between two UHSAS aboard the two aircraft. The average size distribution from both UHSAS and one FIMS in the G1 suggests that UHSAS had an over-counting issue at the size range between 60-90 nm, which was probably due to electrical noise and small signal-to-noise ratio in that size range. Good agreement in the aerosol size distribution measurement provides a "sanity" check for AMS measurements. A CCN closure study suggested that FIMS

25

Atmospheric
Measurement
Techniques
Discussions

745   provides valuable size coverage for better CCN number concentration estimation. Based on the κ-

746   Köhler parameterization, κ_{eff} observed at 500 m above the T3 site is 0.18±0.09, which is similar to

747   the overall mean kappa from long-term ATTO measurements - 0.17±0.06 (Pöhlker et al., 2016).

748   This similarity suggests that there is no significant spatial variability along the downwind transect,

749   although the freshly emitted aerosol particles may have much less hygroscopicity. The difference

750   in the ozone measurement comparison is about 4.1 ppb, which suggests that the bias due to the

751   sampling line loss inside of the G1 gas inlet. The irradiance from the SPN1 unshaded center

752   detector in the G1 was compared with the HALO integrated downward irradiance between 300–

753   1800 nm and achieved a very encouraging agreement with a variance of less than 10%.

754   During the second type of the coordinated flights on September 21 (with cloudy conditions),

755   HALO followed the G1 after take-off from Manus airport; then the two aircraft flew stacked legs

756   relative to each other at different altitudes above the T3 site. For atmospheric state parameters,

757   nearly linear correlations between the G1 and HALO were observed for ambient pressure,

758   temperature, and dew point temperature measurements at an altitude range from ground to around

759   5000 m. Cloud presence affected the measurements of dew point temperature in the G1, resulting

760   in a large discrepancy in the dew point temperature measurement and the derived relative humidity

761   between 2000–3000 m. The horizontal wind had more variation than the rest of the meteorological

762   properties, which is mainly due to the temporal and spatial variability. The aerosol number

763   concentration comparison had an excellent agreement (<15 %) for aerosol particles larger than 10

764   nm counted by the CPC below 2500 m. While the integrated aerosol number concentration from

765   UHSAS showed consistent discrepancy at different altitudes, that suggests the significant temporal

766   and spatial variation of smaller aerosol particles (<100 nm). Although the aircraft-based UHSAS

767   is a challenging instrument to operate, a reasonable size distribution profile comparison was made

768   between both UHSAS and FIMS in the G1. The aerosol concentration measured by AMS

769   instruments showed a mean difference less than 5% above 2500 m during the flight on September

770   21, although due to the ongoing study, the correction factors allowing for correction of data below

771   2500 m are not available yet. The difference between CCN number concentration measured on the

772   two aircraft was on average 20%, and these data show the same altitude behavior as the AMS data.

773   The main contributions to this difference include the difference in aerosol inlet structure, the

774   aerosol loss correction in a constant pressure inlet, and the error propagation of CCN

775   measurements. The ozone and CO vertical profile comparisons show a variation of less than 10%.

Atmospheric
Measurement
Techniques
Discussions

776   The ozone measurement variation is mainly from the systematic bias between two instruments
777   with different operation principles, especially at altitudes higher than 4000 m.

778   Cloud probe comparisons were made for the cloud droplet number concentration between 3–
779   20 µm for the initial comparison between the redundant instruments on the same aircraft. Then the
780   comparison of cloud droplet size distribution between 2-960 µm for a flight leg around 1900 m
781   showed a remarkably good agreement. The major cloud appearance was captured by both aircraft,
782   although the cloud elements observed were affected by the cloud movement with the prevailing
783   wind and the different cloud evolution stages. Furthermore, the relatively short time delay of 7-23
784   minutes between the independent measurements may give a hint for the time scales in which the
785   cloud droplet spectra develop within a convective cloud over the Amazon basin.

786   The above results provide additional information about the reasonableness of measurements
787   for each atmospheric variable. This study confirms the high-quality spatial and temporal dataset
788   with clearly identified uncertainty ranges had been collected from two aircraft and builds a good
789   foundation for further studies on the remote sensing validation and the spatial and temporal
790   evaluation of modeling representation of the atmospheric processing and evolution.

800   **References:**

801   Alfarra, M. R., Coe, H., Allan, J. D., Bower, K. N., Boudries, H., Canagaratna, M. R., Jimenez,
802   J. L., Jayne, J. T., Garforth, A. A., and Li, S.-M.: Characterization of urban and rural organic
803   particulate in the lower Fraser valley using two aerodyne aerosol mass spectrometers, Atmos
804   Environ, 38, 5745-5758, 2004.

805   Andreae, M. O., Acevedo, O. C., Araujo, A., Artaxo, P., Barbosa, C. G. G., Barbosa, H. M. J.,
806   Brito, J., Carbone, S., Chi, X., Cintra, B. B. L., da Silva, N. F., Dias, N. L., Dias, C. Q., Ditas, F.,
807   Ditz, R., Godoi, A. F. L., Godoi, R. H. M., Heimann, M., Hoffmann, T., Kesselmeier, J.,
808   Konemann, T., Kruger, M. L., Lavric, J. V., Manzi, A. O., Lopes, A. P., Martins, D. L.,
809   Mikhailov, E. F., Moran-Zuloaga, D., Nelson, B. W., Nolscher, A. C., Nogueira, D. S., Piedade,
810   M. T. F., Pohlker, C., Poschl, U., Quesada, C. A., Rizzo, L. V., Ro, C. U., Ruckteschler, N., Sa,
811   L. D. A., Sa, M. D., Sales, C. B., dos Santos, R. M. N., Saturno, J., Schongart, J., Sorgel, M., de
812   Souza, C. M., de Souza, R. A. F., Su, H., Targhetta, N., Tota, J., Trebs, I., Trumbore, S., van
813   Eijck, A., Walter, D., Wang, Z., Weber, B., Williams, J., Winderlich, J., Wittmann, F., Wolff, S.,
814   and Yanez-Serrano, A. M.: The Amazon Tall Tower Observatory (ATTO): overview of pilot
815   measurements on ecosystem ecology, meteorology, trace gases, and aerosols, Atmos Chem Phys,
816   15, 10723-10776, 2015.
817   Andreae, M. O., Afchine, A., Albrecht, R., Holanda, B. A., Artaxo, P., Barbosa, H. M. J.,
818   Borrmann, S., Cecchini, M. A., Costa, A., Dollner, M., Fütterer, D., Järvinen, E., Jurkat, T.,
819   Klimach, T., Konemann, T., Knote, C., Krämer, M., Krisna, T., Machado, L. A. T., Mertes, S.,
820   Minikin, A., Pöhlker, C., Pöhlker, M. L., Pöschl, U., Rosenfeld, D., Sauer, D., Schlager, H.,
821   Schnaiter, M., Schneider, J., Schulz, C., Spanu, A., Sperling, V. B., Voigt, C., Walser, A., Wang,
822   J., Weinzierl, B., Wendisch, M., and Ziereis, H.: Aerosol characteristics and particle production
823   in the upper troposphere over the Amazon Basin, Atmos. Chem. Phys., 18, 921-961, 2018.
824   Andreae, M. O., Rosenfeld, D., Artaxo, P., Costa, A., Frank, G., Longo, K., and Silva-Dias, M.:
825   Smoking rain clouds over the Amazon, Science, 303, 1337-1342, 2004.
826   Artaxo, P., Rizzo, L. V., Brito, J. F., Barbosa, H. M. J., Arana, A., Sena, E. T., Cirino, G. G.,
827   Bastos, W., Martin, S. T., and Andreae, M. O.: Atmospheric aerosols in Amazonia and land use
828   change: from natural biogenic to biomass burning conditions, Faraday Discuss, 165, 203-235,
829   2013.
830   Bahreini, R., Dunlea, E. J., Matthew, B. M., Simons, C., Docherty, K. S., DeCarlo, P. F.,
831   Jimenez, J. L., Brock, C. A., and Middlebrook, A. M.: Design and operation of a pressure-
832   controlled inlet for airborne sampling with an aerodynamic aerosol lens, Aerosol Sci Tech, 42,
833   465-471, 2008.
834   Bhattu, D. and Tripathi, S. N.: CCN closure study: Effects of aerosol chemical composition and
835   mixing state, J Geophys Res-Atmos, 120, 766-783, 2015.
836   Brenguier, J. L., Bachalo, W. D., Chuang, P. Y., Esposito, B. M., Fugal, J., Garrett, T., Gayet, J.
837   F., Gerber, H., Heymsfield, A., and Kokhanovsky, A.: In situ measurements of cloud and
838   precipitation particles, Airborne Measurements for Environmental Research: Methods and
839   Instruments, 2013. 225-301, 2013.
840   Broekhuizen, K., Chang, R.-W., Leaitch, W., Li, S.-M., and Abbatt, J.: Closure between
841   measured and modeled cloud condensation nuclei (CCN) using size-resolved aerosol
842   compositions in downtown Toronto, Atmos Chem Phys, 6, 2513-2524, 2006a.
843   Broekhuizen, K., Chang, R. Y. W., Leaitch, W. R., Li, S. M., and Abbatt, J. P. D.: Closure
844   between measured and modeled cloud condensation nuclei (CCN) using size-resolved aerosol
845   compositions in downtown Toronto, Atmos Chem Phys, 6, 2513-2524, 2006b.
846   Cai, Y., Montague, D. C., Mooiweer-Bryan, W., and Deshler, T.: Performance characteristics of
847   the ultra high sensitivity aerosol spectrometer for particles between 55 and 800 nm: Laboratory
848   and field studies, J Aerosol Sci, 39, 759-769, 2008.
849   Chang, R. Y. W., Slowik, J. G., Shantz, N. C., Vlasenko, A., Liggio, J., Sjostedt, S. J., Leaitch,
850   W. R., and Abbatt, J. P. D.: The hygroscopicity parameter (kappa) of ambient organic aerosol at

Atmospheric
Measurement
Techniques
Discussions

851   a field site subject to biogenic and anthropogenic influences: relationship to degree of aerosol
852   oxidation, Atmos Chem Phys, 10, 5047-5064, 2010.
853   Costa, A., Meyer, J., Afchine, A., Luebke, A., Günther, G., Dorsey, J. R., Gallagher, M. W.,
854   Ehrlich, A., Wendisch, M., and Baumgardner, D.: Classification of Arctic, midlatitude and
855   tropical clouds in the mixed-phase temperature regime, Atmos Chem Phys, 17, 12219-12238,
856   2017.
857   Davidson, E. A., de Araujo, A. C., Artaxo, P., Balch, J. K., Brown, I. F., Bustamante, M. M. C.,
858   Coe, M. T., DeFries, R. S., Keller, M., Longo, M., Munger, J. W., Schroeder, W., Soares, B. S.,
859   Souza, C. M., and Wofsy, S. C.: The Amazon basin in transition (vol 481, pg 321, 2012), Nature,
860   483, 232-232, 2012.
861   DeCarlo, P. F., Kimmel, J. R., Trimborn, A., Northway, M. J., Jayne, J. T., Aiken, A. C., Gonin,
862   M., Fuhrer, K., Horvath, T., Docherty, K. S., Worsnop, D. R., and Jimenez, J. L.: Field-
863   deployable, high-resolution, time-of-flight aerosol mass spectrometer, Anal Chem, 78, 8281-
864   8289, 2006.
865   Dolgos, G. and Martins, J. V.: Polarized Imaging Nephelometer for in situ airborne
866   measurements of aerosol light scattering, Optics express, 22, 21972-21990, 2014.
867   Duplissy, J., Gysel, M., Alfarra, M. R., Dommen, J., Metzger, A., Prevot, A. S. H., Weingartner,
868   E., Laaksonen, A., Raatikainen, T., Good, N., Turner, S. F., McFiggans, G., and Baltensperger,
869   U.: Cloud forming potential of secondary organic aerosol under near atmospheric conditions,
870   Geophys Res Lett, 35, 2008.
871   Faber, S., French, J. R., and Jackson, R.: Laboratory and in-flight evaluation of measurement
872   uncertainties from a commercial Cloud Droplet Probe (CDP), Atmos Meas Tech, 11, 3645-3659,
873   2018.
874   Fan, J., Rosenfeld, D., Zhang, Y., Giangrande, S. E., Li, Z., Machado, L. A., Martin, S. T., Yang,
875   Y., Wang, J., and Artaxo, P.: Substantial convection and precipitation enhancements by ultrafine
876   aerosol particles, Science, 359, 411-418, 2018.
877   Giez, A., Mallaun, C., Zöger, M., Dörnbrack, A., and Schumann, U.: Static pressure from aircraft
878   trailing-cone measurements and numerical weather-prediction analysis, J Aircraft, 54, 1728-
879   1737, 2017.
880   Gunthe, S., King, S., Rose, D., Chen, Q., Roldin, P., Farmer, D., Jimenez, J., Artaxo, P.,
881   Andreae, M., and Martin, S.: Cloud condensation nuclei in pristine tropical rainforest air of
882   Amazonia: size-resolved measurements and modeling of atmospheric aerosol composition and
883   CCN activity, Atmos Chem Phys, 9, 7551-7575, 2009.
884   Guyon, P., Boucher, O., Graham, B., Beck, J., Mayol-Bracero, O. L., Roberts, G. C., Maenhaut,
885   W., Artaxo, P., and Andreae, M. O.: Refractive index of aerosol particles over the Amazon
886   tropical forest during LBA-EUSTACH 1999, J Aerosol Sci, 34, 883-907, 2003.
887   Jayne, J. T., Leard, D. C., Zhang, X. F., Davidovits, P., Smith, K. A., Kolb, C. E., and Worsnop,
888   D. R.: Development of an aerosol mass spectrometer for size and composition analysis of
889   submicron particles, Aerosol Sci Tech, 33, 49-70, 2000.
890   Keller, M., Bustamante, M., Gash, J., and Dias, P. S. (Eds.): Amazonia and Global Change,
891   American Geophysical Union, Washington, DC, 2009.
892   Kleinman, L. I., Daum, P. H., Lee, Y. N., Senum, G. I., Springston, S. R., Wang, J., Berkowitz,
893   C., Hubbe, J., Zaveri, R. A., and Brechtel, F. J.: Aircraft observations of aerosol composition and
894   ageing in New England and Mid-Atlantic States during the summer 2002 New England Air
895   Quality Study field campaign, Journal of Geophysical Research: Atmospheres, 112, 2007.

896   Klingebiel, M., de Lozar, A., Molleker, S., Weigel, R., Roth, A., Schmidt, L., Meyer, J., Ehrlich,
897   A., Neuber, R., Wendisch, M., and Borrmann, S.: Arctic low-level boundary layer clouds: in situ
898   measurements and simulations of mono- and bimodal supercooled droplet size distributions at
899   the top layer of liquid phase clouds, Atmos Chem Phys, 15, 617-631, 2015.
900   Kotchenruther, R. A. and Hobbs, P. V.: Humidification factors of aerosols from biomass burning
901   in Brazil, J Geophys Res-Atmos, 103, 32081-32089, 1998.
902   Krautstrunk, M. and Giez, A.: The transition from FALCON to HALO era airborne atmospheric
903   research. In: Atmospheric Physics, Springer, 2012.
904   Krisna, T. C., Wendisch, M., Ehrlich, A., Jäkel, E., Werner, F., Weigel, R., Borrmann, S.,
905   Mahnke, C., Pöschl, U., Andreae, M. O., Voigt, C., and Machado, L. A. T.: Comparing airborne
906   and satellite retrievals of cloud optical thickness and particle effective radius using a spectral
907   radiance ratio technique: two case studies for cirrus and deep convective clouds, Atmos. Chem.
908   Phys., 18, 4439-4462, 2018.
909   Kuhn, U., Ganzeveld, L., Thielmann, A., Dindorf, T., Schebeske, G., Welling, M., Sciare, J.,
910   Roberts, G., Meixner, F. X., Kesselmeier, J., Lelieveld, J., Kolle, O., Ciccioli, P., Lloyd, J.,
911   Trentmann, J., Artaxo, P., and Andreae, M. O.: Impact of Manaus City on the Amazon Green
912   Ocean atmosphere: ozone production, precursor sensitivity and aerosol load, Atmos Chem Phys,
913   10, 9251-9282, 2010.
914   Kulkarni, P. and Wang, J.: New fast integrated mobility spectrometer for real-time measurement
915   of aerosol size distribution - I: Concept and theory, J Aerosol Sci, 37, 1303-1325, 2006a.
916   Kulkarni, P. and Wang, J.: New fast integrated mobility spectrometer for real-time measurement
917   of aerosol size distribution: II. Design, calibration, and performance characterization, J Aerosol
918   Sci, 37, 1326-1339, 2006b.
919   Kupc, A., Williamson, C., Wagner, N. L., Richardson, M., and Brock, C. A.: Modification,
920   calibration, and performance of the Ultra-High Sensitivity Aerosol Spectrometer for particle size
921   distribution and volatility measurements during the Atmospheric Tomography Mission (ATom)
922   airborne campaign, Atmos. Meas. Tech., 11, 369-383, 2018.
923   Lambe, A. T., Onasch, T. B., Massoli, P., Croasdale, D. R., Wright, J. P., Ahern, A. T.,
924   Williams, L. R., Worsnop, D. R., Brune, W. H., and Davidovits, P.: Laboratory studies of the
925   chemical composition and cloud condensation nuclei (CCN) activity of secondary organic
926   aerosol (SOA) and oxidized primary organic aerosol (OPOA), Atmos Chem Phys, 11, 8913-
927   8928, 2011.
928   Lance, S., Brock, C. A., Rogers, D., and Gordon, J. A.: Water droplet calibration of the Cloud
929   Droplet Probe (CDP) and in-flight performance in liquid, ice and mixed-phase clouds during
930   ARCPAC, Atmospheric Measurement Techniques, 3, 1683-1706, 2010.
931   Lawson, R.: Effects of ice particles shattering on the 2D-S probe, Atmos Meas Tech, 4, 1361-
932   1381, 2011.
933   Lawson, R. P., O'Connor, D., Zmarzly, P., Weaver, K., Baker, B., Mo, Q., and Jonsson, H.: The
934   2D-S (stereo) probe: Design and preliminary tests of a new airborne, high-speed, high-resolution
935   particle imaging probe, J Atmos Ocean Tech, 23, 1462-1477, 2006.
936   Liu, B. Y. and Pui, D. Y.: A submicron aerosol standard and the primary, absolute calibration of
937   the condensation nuclei counter, Journal of Colloid and Interface Science, 47, 155-171, 1974.
938   Long;, C. N., Bucholtz;, A., Jonsson;, H., Schmid;, B., Vogelmann;, A., and Wood, J.: A Method
939   of Correcting for Tilt from Horizontal in Downwelling Shortwave Irradiance Measurements on
940   Moving Platforms, The Open Atmospheric Science Journal, 4, 78-87, 2010.

941   Luebke, A. E., Afchine, A., Costa, A., Grooss, J. U., Meyer, J., Rolf, C., Spelten, N., Avallone,
942   L. M., Baumgardner, D., and Kramer, M.: The origin of midlatitude ice clouds and the resulting
943   influence on their microphysical properties, Atmos Chem Phys, 16, 5793-5809, 2016.
944   Martin, S., Artaxo, P., Machado, L., Manzi, A., Souza, R., Schumacher, C., Wang, J., Andreae,
945   M., Barbosa, H., and Fan, J.: Introduction: observations and modeling of the Green Ocean
946   Amazon (GoAmazon2014/5), Atmos Chem Phys, 16, 2016a.
947   Martin, S. T., Artaxo, P., Machado, L., Manzi, A. O., Souza, R. A. F., Schumacher, C., Wang, J.,
948   Biscaro, T., Brito, J., Calheiros, A., Jardine, K., Medeiros, A., Portela, B., de Sa, S. S., Adachi,
949   K., Aiken, A. C., Albrecht, R., Alexander, L., Andreae, M. O., Barbosa, M. J., Buseck, P.,
950   Chand, D., Comstock, J. M., Day, D. A., Dubey, M., Fan, J., Fast, J., Fisch, G., Fortner, E.,
951   Giangrande, S., Gilles, M., Goldststein, A. H., Guenther, A., Hubbe, J., Jensen, M., Jimenez, J.
952   L., Keutsch, F. N., Kim, S., Kuang, C., Laskskin, A., McKinney, K., Mei, F., Miller, M.,
953   Nascimento, R., Pauliquevis, T., Pekour, M., Peres, J., Petaja, T., Pohlker, C., Poschl, U., Rizzo,
954   L., Schmid, B., Shilling, J. E., Dias, M. A. S., Smith, J. N., Tomlmlinson, J. M., Tota, J., and
955   Wendisch, M.: The Green Ocean Amazon Experiment (Goamazon2014/5) Observes Pollution
956   Affecting Gases, Aerosols, Clouds, and Rainfall over the Rain Forest, B Am Meteorol Soc, 98,
957   981-997, 2017.
958   Martin, S. T., Artaxo, P., Machado, L. A. T., Manzi, A. O., Souza, R. A. F., Schumacher, C.,
959   Wang, J., Andreae, M. O., Barbosa, H. M. J., Fan, J., Fisch, G., Goldstein, A. H., Guenther, A.,
960   Jimenez, J. L., Poschl, U., Dias, M. A. S., Smith, J. N., and Wendisch, M.: Introduction:
961   Observations and Modeling of the Green Ocean Amazon (GoAmazon2014/5), Atmos Chem
962   Phys, 16, 4785-4797, 2016b.
963   Mei, F., Hayes, P. L., Ortega, A., Taylor, J. W., Allan, J. D., Gilman, J., Kuster, W., de Gouw, J.,
964   Jimenez, J. L., and Wang, J.: Droplet activation properties of organic aerosols observed at an
965   urban site during CalNex-LA, J Geophys Res-Atmos, 118, 2903-2917, 2013a.
966   Mei, F., Setyan, A., Zhang, Q., and Wang, J.: CCN activity of organic aerosols observed
967   downwind of urban emissions during CARES, Atmos Chem Phys, 13, 12155-12169, 2013b.
968   Middlebrook, A. M., Bahreini, R., Jimenez, J. L., and Canagaratna, M. R.: Evaluation of
969   composition-dependent collection efficiencies for the aerodyne aerosol mass spectrometer using
970   field data, Aerosol Sci Tech, 46, 258-271, 2012.
971   Minikin, A., Sauer, D., Ibrahim, A., Franke, H., Röschenthaler, T., Fütterer, D. A., and Petzold,
972   A.: The HALO Submicrometer Aerosol Inlet (HASI): Design concept and first characterization,
973   1st HALO symposium: Airborne Research with HALO: Achievements and Prospects,
974   Oberpfaffenhofen, Deutschland,, 2017. 2017.
975   Molleker, S., Borrmann, S., Schlager, H., Luo, B., Frey, W., Klingebiel, M., Weigel, R., Ebert,
976   M., Mitev, V., Matthey, R., Woiwode, W., Oelhaf, H., Dornbrack, A., Stratmann, G., Grooss, J.
977   U., Gunther, G., Vogel, B., Muller, R., Kramer, M., Meyer, J., and Cairo, F.: Microphysical
978   properties of synoptic-scale polar stratospheric clouds: in situ measurements of unexpectedly
979   large HNO3-containing particles in the Arctic vortex, Atmos Chem Phys, 14, 10785-10801,
980   2014.
981   Moran-Zuloaga, D., Ditas, F., Walters, D., Saturno, J., Brito, J., Carbone, S., Chi, X. G., de
982   Angelis, I. H., Baars, H., Godoi, R. H. M., Heese, B., Holanda, B. A., Lavric, J. V., Martin, S. T.,
983   Ming, J., Pohlker, M. L., Ruckteschler, N., Su, H., Wang, Y. Q., Wang, Q. Q., Wang, Z. B.,
984   Weber, B., Wolff, S., Artaxo, P., Poschl, U., Andreae, M. O., and Pohlker, C.: Long-term study
985   on coarse mode aerosols in the Amazon rain forest with the frequent intrusion of Saharan dust
986   plumes, Atmos Chem Phys, 18, 10055-10088, 2018.

Atmospheric
Measurement
Techniques
Discussions

Open Access

EGU

987 Olfert, J. S., Kulkarni, P., and Wang, J.: Measuring aerosol size distributions with the fast
988 integrated mobility spectrometer, J Aerosol Sci, 39, 940-956, 2008.
989 Petzold, A., Marsh, R., Johnson, M., Miller, M., Sevcenco, Y., Delhaye, D., Ibrahim, A.,
990 Williams, P., Bauer, H., Crayford, A., Bachalo, W. D., and Raper, D.: Evaluation of Methods for
991 Measuring Particulate Matter Emissions from Gas Turbines, Environ Sci Technol, 45, 3562-
992 3568, 2011.
993 Pöhlker, M. L., Ditas, F., Saturno, J., Klimach, T., de Angelis, I. H., Araujo, A. C., Brito, J.,
994 Carbone, S., Cheng, Y. F., Chi, X. G., Ditz, R., Gunthe, S. S., Holanda, B. A., Kandler, K.,
995 Kesselmeier, J., Konemann, T., Kruger, O. O., Lavric, J. V., Martin, S. T., Mikhailov, E., Moran-
996 Zuloaga, D., Rizzo, L. V., Rose, D., Su, H., Thalman, R., Walter, D., Wang, J., Wolff, S.,
997 Barbosa, H. M. J., Artaxo, P., Andreae, M. O., Pöschl, U., and Pöhlker, C.: Long-term
998 observations of cloud condensation nuclei over the Amazon rain forest - Part 2: Variability and
999 characteristics of biomass burning, long-range transport, and pristine rain forest aerosols, Atmos
1000 Chem Phys, 18, 10289-10331, 2018.
1001 Pöhlker, M. L., Pöhlker, C., Ditas, F., Klimach, T., de Angelis, I. H., Araujo, A., Brito, J.,
1002 Carbone, S., Cheng, Y. F., Chi, X. G., Ditz, R., Gunthe, S. S., Kesselmeier, J., Konemann, T.,
1003 Lavric, J. V., Martin, S. T., Mikhailov, E., Moran-Zuloaga, D., Rose, D., Saturno, J., Su, H.,
1004 Thalman, R., Walter, D., Wang, J., Wolff, S., Barbosa, H. M. J., Artaxo, P., Andreae, M. O., and
1005 Poschl, U.: Long-term observations of cloud condensation nuclei in the Amazon rain forest - Part
1006 1: Aerosol size distribution, hygroscopicity, and new model parametrizations for CCN
1007 prediction, Atmos Chem Phys, 16, 15709-15740, 2016.
1008 Pöschl, U., Martin, S., Sinha, B., Chen, Q., Gunthe, S., Huffman, J., Borrmann, S., Farmer, D.,
1009 Garland, R., and Helas, G.: Rainforest aerosols as biogenic nuclei of clouds and precipitation in
1010 the Amazon, Science, 329, 1513-1516, 2010.
1011 Poschl, U., Martin, S. T., Sinha, B., Chen, Q., Gunthe, S. S., Huffman, J. A., Borrmann, S.,
1012 Farmer, D. K., Garland, R. M., Helas, G., Jimenez, J. L., King, S. M., Manzi, A., Mikhailov, E.,
1013 Pauliquevis, T., Petters, M. D., Prenni, A. J., Roldin, P., Rose, D., Schneider, J., Su, H., Zorn, S.
1014 R., Artaxo, P., and Andreae, M. O.: Rainforest aerosols as biogenic nuclei of clouds and
1015 precipitation in the Amazon, Science, 329, 1513-1516, 2010.
1016 Rissler, J., Swietlicki, E., Zhou, J., Roberts, G., Andreae, M. O., Gatti, L., and Artaxo, P.:
1017 Physical properties of the sub-micrometer aerosol over the Amazon rain forest during the wet-to-
1018 dry season transition-comparison of modeled and measured CCN concentrations, Atmos Chem
1019 Phys, 4, 2119-2143, 2004.
1020 Roberts, G. C., Andreae, M. O., Zhou, J., and Artaxo, P.: Cloud condensation nuclei in the
1021 Amazon Basin:"Marine" conditions over a continent?, Geophys Res Lett, 28, 2807-2810, 2001.
1022 Roberts, G. C., Artaxo, P., Zhou, J., Swietlicki, E., and Andreae, M. O.: Sensitivity of CCN
1023 spectra on chemical and physical properties of aerosol: A case study from the Amazon Basin,
1024 Journal of Geophysical Research: Atmospheres, 107, LBA 37-31-LBA 37-18, 2002.
1025 Rose, D., Gunthe, S., Mikhailov, E., Frank, G., Dusek, U., Andreae, M. O., and Pöschl, U.:
1026 Calibration and measurement uncertainties of a continuous-flow cloud condensation nuclei
1027 counter (DMT-CCNC): CCN activation of ammonium sulfate and sodium chloride aerosol
1028 particles in theory and experiment, Atmos Chem Phys, 8, 1153-1179, 2008.
1029 Salati, E. and Vose, P. B.: Amazon basin: a system in equilibrium, Science, 225, 129-138, 1984.
1030 Schmid, B., Tomlinson, J. M., Hubbe, J. M., Comstock, J. M., Mei, F., Chand, D., Pekour, M. S.,
1031 Kluzek, C. D., Andrews, E., Biraud, S. C., and Mcfarquhar, G. M.: The Doe Arm Aerial Facility,
1032 B Am Meteorol Soc, 95, 723-+, 2014.

Atmospheric
Measurement
Techniques
Discussions

Open Access

Schulz, C., Schneider, J., Amorim Holanda, B., Appel, O., Costa, A., de Sá, S. S., Dreiling, V.,
Fütterer, D., Jurkat-Witschas, T., Klimach, T., Knote, C., Krämer, M., Martin, S. T., Mertes, S.,
Pöhlker, M. L., Sauer, D., Voigt, C., Walser, A., Weinzierl, B., Ziereis, H., Zöger, M., Andreae,
M. O., Artaxo, P., Machado, L. A. T., Pöschl, U., Wendisch, M., and Borrmann, S.: Aircraft-
based observations of isoprene-epoxydiol-derived secondary organic aerosol (IEPOX-SOA) in
the tropical upper troposphere over the Amazon region, Atmos. Chem. Phys., 18, 14979-15001,
2018.
Shilling, J. E., Pekour, M. S., Fortner, E. C., Artaxo, P., Sá, S. d., Hubbe, J. M., Longo, K. M.,
Machado, L. A., Martin, S. T., and Springston, S. R.: Aircraft observations of the chemical
composition and aging of aerosol in the Manaus urban plume during GoAmazon 2014/5, Atmos
Chem Phys, 18, 10773-10797, 2018.
Shilling, J. E., Zaveri, R. A., Fast, J. D., Kleinman, L., Alexander, M., Canagaratna, M. R.,
Fortner, E., Hubbe, J. M., Jayne, J. T., and Sedlacek, A.: Enhanced SOA formation from mixed
anthropogenic and biogenic emissions during the CARES campaign, Atmos Chem Phys, 13,
2091-2113, 2013.
Thalman, R., de Sa, S. S., Palm, B. B., Barbosa, H. M. J., Pohlker, M. L., Alexander, M. L.,
Brito, J., Carbone, S., Castillo, P., Day, D. A., Kuang, C. G., Manzi, A., Ng, N. L., Sedlacek, A.
J., Souza, R., Springston, S., Watson, T., Pohlker, C., Poschl, U., Andreae, M. O., Artaxo, P.,
Jimenez, J. L., Martin, S. T., and Wang, J.: CCN activity and organic hygroscopicity of aerosols
downwind of an urban region in central Amazonia: seasonal and diel variations and impact of
anthropogenic emissions, Atmos Chem Phys, 17, 11779-11801, 2017.
Wang, J.: A fast integrated mobility spectrometer with wide dynamic size range: Theoretical
analysis and numerical simulation, J Aerosol Sci, 40, 890-906, 2009.
Wang, J., Krejci, R., Giangrande, S., Kuang, C., Barbosa, H. M., Brito, J., Carbone, S., Chi, X.,
Comstock, J., Ditas, F., Lavric, J., Manninen, H. E., Mei, F., Moran-Zuloaga, D., Pohlker, C.,
Pohlker, M. L., Saturno, J., Schmid, B., Souza, R. A., Springston, S. R., Tomlinson, J. M., Toto,
T., Walter, D., Wimmer, D., Smith, J. N., Kulmala, M., Machado, L. A., Artaxo, P., Andreae, M.
O., Petaja, T., and Martin, S. T.: Amazon boundary layer aerosol concentration sustained by
vertical transport during rainfall, Nature, 539, 416-419, 2016.
Wang, J., Lee, Y.-N., Daum, P. H., Jayne, J., and Alexander, M.: Effects of aerosol organics on
cloud condensation nucleus (CCN) concentration and first indirect aerosol effect, Atmos Chem
Phys, 8, 6325-6339, 2008.
Webster, C. and Freudinger, L.: Interagency Working Group for Airborne Data and
Telecommunications, 2018.
Wendisch, M. and Brenguier, J.-L.: Airborne measurements for environmental research: methods
and instruments, John Wiley & Sons, 2013.
Wendisch, M., Coe, H., Baumgardner, D., Brenguier, J.-L., Dreiling, V., Fiebig, M., Formenti,
P., Hermann, M., Krämer, M., Levin, Z., Maser, R., Mathieu, E., Nacass, P., Noone, K.,
Osborne, S., Schneider, J., Schütz, L., Schwarzenböck, A., Stratmann, F., and Wilson, J. C.:
Aircraft Particle Inlets: State-of-the-Art and Future Needs, B Am Meteorol Soc, 85, 89-92, 2004.
Wendisch, M., Keil, A., and Korolev, A. V.: FSSP characterization with monodisperse water
droplets, Journal of Atmospheric and Oceanic Technology, 13, 1152-1165, 1996.
Wendisch, M., Müller, D., Schell, D., and Heintzenberg, J.: An airborne spectral albedometer
with active horizontal stabilization, J Atmos Ocean Tech, 18, 1856-1866, 2001.
Wendisch, M., Poschl, U., Andreae, M. O., Machado, L. A. T., Albrecht, R., Schlager, H.,
Rosenfeld, D., Martin, S. T., Abdelmomonem, A., Afchine, A., Araujo, A. C., Artaxo, P.,

33

Atmospheric
Measurement
Techniques
Discussions

1079   Aufmhoff, H., Barbosa, H. M. J., Borrmann, S., Braga, R., Buchholz, B., Cecchini, M. A., Costa,
1080   A., Curtius, J., Dollner, M., Dorf, M., Dreiling, V., Ebert, V., Ehrlich, A., Ewald, F., Fisch, G.,
1081   Fix, A., Frank, F., Futterer, D., Heckl, C., Heidelberg, F., Huneke, T., Jakel, E., Jarvinen, E.,
1082   Jurkat, T., Kanter, S., Kastner, U., Kenntner, M., Kesselmeier, J., Klimach, T., Knecht, M., Kohl,
1083   R., Kolling, T., Kramer, M., Kruger, M., Krisna, T. C., Lavric, J. V., Longo, K., Mahnke, C.,
1084   Manzi, A. O., Mayer, B., Mertes, S., Minikin, A., Molleker, S., Munch, S., Nillius, B.,
1085   Pfeilsticker, K., Pohlker, C., Roiger, A., Rose, D., Rosenowow, D., Sauer, D., Schnaiter, M.,
1086   Schneider, J., Schulz, C., de Souza, R. A. F., Spanu, A., Stock, P., Vila, D., Voigt, C., Walser,
1087   A., Walter, D., Weigel, R., Weinzierl, B., Werner, F., Yamasoe, M. A., Ziereis, H., Zinner, T.,
1088   and Zoger, M.: ACRIDICON-CHUVA CAMPAIGN Studying Tropical Deep Convective
1089   Clouds and Precipitation over Amazonia Using the New German Research Aircraft HALO, B
1090   Am Meteorol Soc, 97, 1885-1908, 2016.
1091   Zaveri, R. A., Berkowitz, C. M., Brechtel, F. J., Gilles, M. K., Hubbe, J. M., Jayne, J. T.,
1092   Kleinman, L. I., Laskin, A., Madronich, S., and Onasch, T. B.: Nighttime chemical evolution of
1093   aerosol and trace gases in a power plant plume: Implications for secondary organic nitrate and
1094   organosulfate aerosol formation, NO3 radical chemistry, and N2O5 heterogeneous hydrolysis,
1095   Journal of Geophysical Research: Atmospheres, 115, 2010.

1096

1097

1098   Table 1. List of compared measurements and corresponding instruments deployed aboard the G1
1099   and HALO during GoAmazon2014/5. The acronyms are defined in a table at the end of this
1100   paper. Dp indicates the particle diameter. ☐Dp refers to the size resolution.

Measurement Variables	Instruments deployed on the G1 (Martin et al., 2016b; Schmid et al., 2014)	Instruments deployed on HALO (Wendisch et al., 2016)
Static Pressure	Rosemount (1201F1), 0-1400 hPa	Instrumented nose boom tray (DLR development), 0-1400 hPa
Static air temperature	Rosemount E102AL/510BF -50 to +50 °C	Total Air Temperature (TAT) inlet (Goodrich/Rosemount type 102) with an open wire resistance temperature sensor (PT100), -70 to +50 °C
Dewpoint temperature	Chilled mirror hygrometer 1011B -40 to +50 °C	Derived from the water-vapor mixing ratio, which is measured by a tunable diode laser (TDL) system (DLR development), 5-40000 ppmv
3-D wind	Aircraft Integrated Meteorological Measurement System 20 (AIMMS-20)	Instrumented nose boom tray (DLR development) with an air data probe (Goodrich/Rosemount) 858AJ and high-precision Inertial Reference System (IGI IMU-IIe)
Particle number concentration	CPC, cut off size (D_p) =10 nm	CPC, cut off size (D_p) =10 nm
Size distribution*	UHSAS-A, 60-1000 nm. FIMS, 20 nm – 500 nm	UHSAS-A, 60-1000 nm.
Non-Refractory particle chemical composition	HR-ToF-AMS: Organics, Sulfate, Nitrate, Ammonium, Chloride, 60-1000 nm	C-ToF-AMS: Organics, Sulfate, Nitrate, Ammonium, Chloride, 60-1000 nm
CCN concentration	CCN-200, SS= 0.25, 0.5%	CCN-200, SS= 0.13-0.53%
Gas phase concentration	N2O/CO and Ozone Analyzer, CO, O_3 concentration, precision 2 ppb	N2O/CO and Ozone Analyzer, CO, O_3 concentration, precision 2 ppb
Cloud properties*	CDP, 2-50 μm, ΔD_p=1-2 μm	CCP-CDP, 2.5-46 mm, ΔD_p=1-2 μm
	FCDP, 2-50 μm, ΔD_p=1-2 μm	NIXE-CAS: 0.61 -52.5 μm
	2DS, 10-1000 μm	NIXE-CIPgs, 15-960 μm
		CCP-CIPgs: 15-960 μm
Radiation	SPN1 downward irradiance, 400-2700 nm	SMART Albedometer, downward spectral irradiance, 300-2200 nm

1101   *for an individual flight, the size range may vary.

1102

Atmospheric
Measurement
Techniques
Discussions

1103

1104   Table 2. Summary of the total data points compared between the G1 and HALO instruments.

	SEP 9, 2014		SEP 21, 2014	
	G1	HALO	G1	HALO
Atmospheric parameters	2815	2815	7326	12065
Gas phase, CO	N/A	N/A	7326	12065
Gas phase, Ozone	2815	2815	7110	11766
CPC	2043	2043	8466	11646
UHSAS (FIMS)	2031	2031	5841 (9405)	828
AMS	N/A	N/A	587	818
CCNc	663	531	7982	4546
G1: CDP(FCDP) HALO: CCP-CDP (NIXE-CAS)	N/A	N/A	3627(4439)	2051(2260)
G1: 2DS HALO: CCP-CIPgs (NIXE-CIPgs)	N/A	N/A	2280	2261 (2260)
RAD	1355	1355	N/A	N/A

1105

1106

Atmospheric
Measurement
Techniques
Open Access
EGU
Discussions

1107

1108 Table 3. Summary of basic statistics of data between in situ measurements

Variables	G1				HALO					
	min	max	mean	std	min	max	mean	std	slope	R^2
T, K	297.7	300.2	298.9	0.5	297.2	299.4	298.4	0.4	1.002	Neg.
P, hPa	955	965	960.1	1.5	958	964.9	961.8	0.9	0.998	Neg.
WSpd, m/s	0.3	8.9	3.4	1.2	0.3	7.7	3.8	1.1	0.998	Neg.
T_{dew}, *k*	293	296.5	295.0	0.5	292.9	294.9	294.0	0.3	0.996	Neg.
Ozone, ppb	0.5	58.8	22.2	9.3	18.3	50.8	26.3	6.6	1.082	0.9401
CPC, cm^{-3}	696.0	3480.6	1591.3	568.7	687.4	2639.4	1313.8	473.5	0.819	0.8508
UHSAS, cm^{-3}	78.2	1118.	645.5	116.3	504.1	1622.2	756.3	138.6	1.165	0.8193
CCNc (κ)	0.010	0.347	0.1855	0.067	0.012	0.394	0.1890	0.083	0.8937	Neg.

Comparison of the coordinated flight on Sep. 9

1109

1110

1111   Table 4. List of compared measurements ranges and measurement variances caused by the spatial

1112   variation during the field campaign.

Measurement Variables	Measured Range during the Field Campaign	Measurement Variances between the Two Aircraft
Static Pressure	500 – 1010 hPa	< 1 %
Static air temperature	272 – 310 K	< 1%
Dewpoint temperature	230 -300 K	Without clouds, <1% With clouds, the measurement from the G1 can be up to 5% lower than that of HALO
3-D wind	1-15 m/s	< 40%
Particle number concentration	500 – 15,000 cm^{-3}	< 20% for CPC, <50% for UHSAS (size dependent)
Non-Refractory particle chemical composition	< 10 $\mu g \cdot m^{-3}$	< 10% above 2500 m Up to 50% below 2500 m
CCN concentration	SS=0.25%, 100 – 2000 cm^{-3}	< 10% above 2500 m Up to 50% below 2500 m
Gas phase concentration	Ozone: 15-75 ppb CO: 50-200 ppb	Ozone: < 25% CO: < 15%
Cloud droplet number concentration	3- 20 μm	<50 %
Downward irradiance	200 -1500 $W \cdot m^{-2}$	< 10%

1113

1114

1115

1116

(a)   (b)
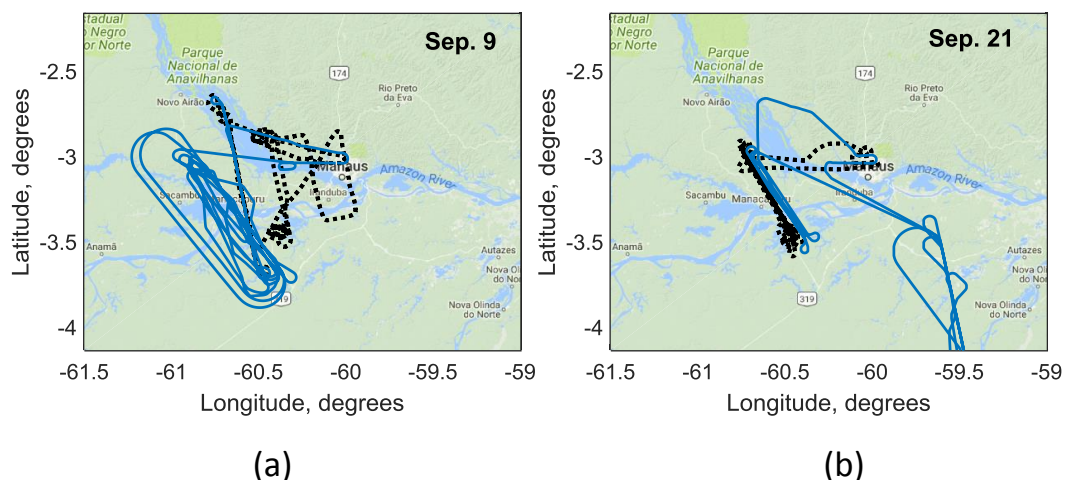
Figure 1. Coordinated flight tracks for September 9 (a) and September 21 (b). The black dotted
line is the flight track of the G1, and the blue line is the flight track of HALO.

1117

1118

1119

1120

Atmospheric
Measurement
Techniques
Discussions
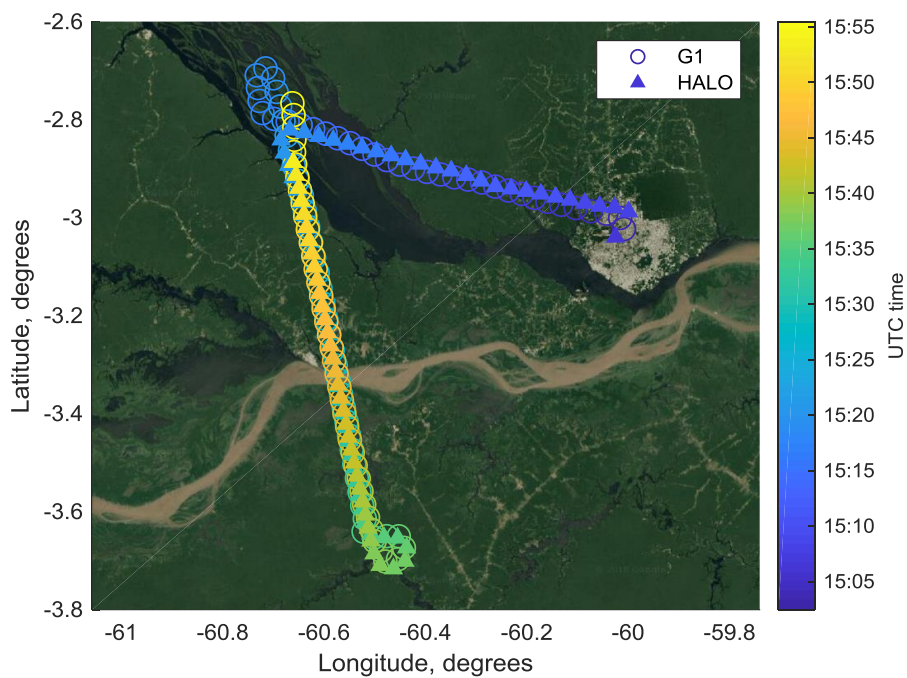
1121

Figure 2. Time-colored flight track of the G1 (circle) and HALO (triangle) on September 9 during

a cloud-free coordinated flight at 500 m above sea level (50 m apart as the closest distance).

Atmospheric
Measurement
Techniques
Discussions

1124

(a)   (b)
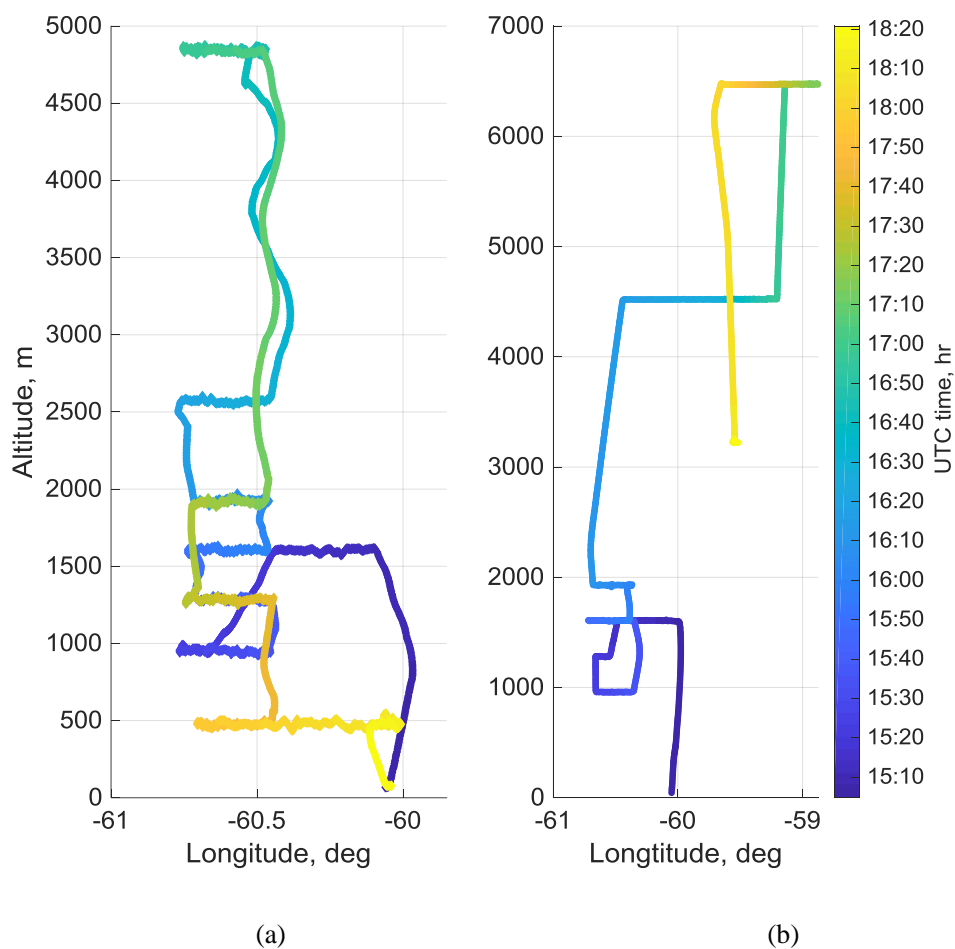
Figure 3. Time-colored flight profile of the G1 (a) and HALO (b) on September 21, during a
coordinated flight.
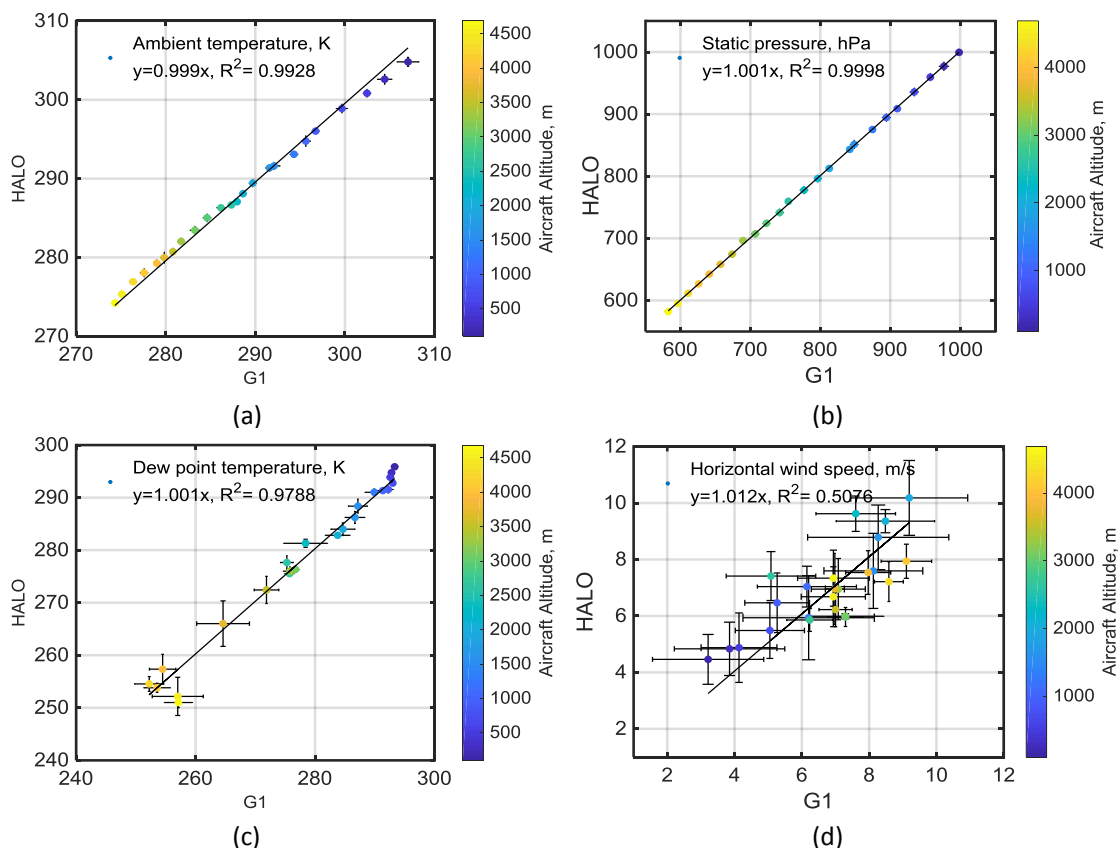
Figure 4. Aircraft altitude-colored plots of (a) ambient temperature, (b) static pressure, (c) dew point temperature, and (d) horizontal wind speed observed by the G1 and HALO on September 21.

Atmospheric
Measurement
Techniques
Open Access
Discussions

EGU
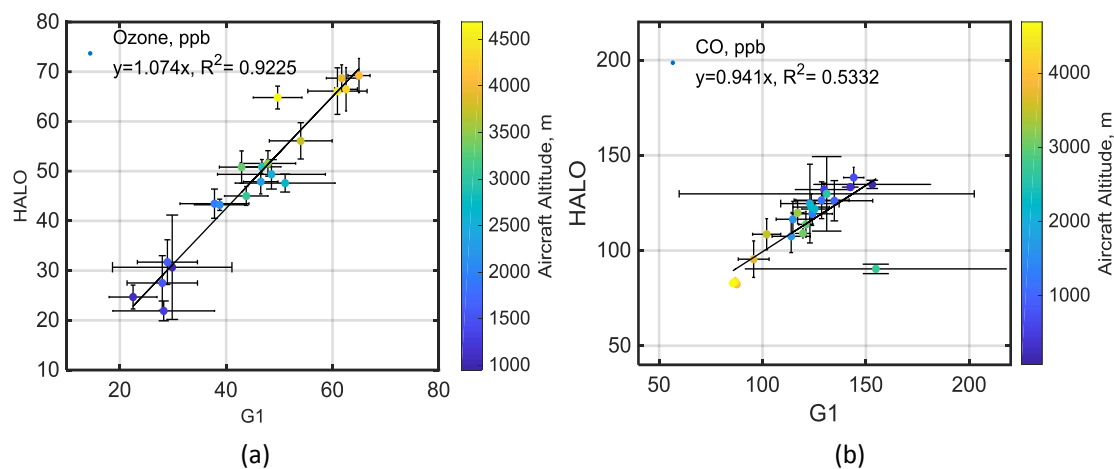
1133

1134   Figure 5. Aircraft altitude-colored plots of trace gas (a) Ozone, (b) CO, for the coordinated flight

1135   on September 21.
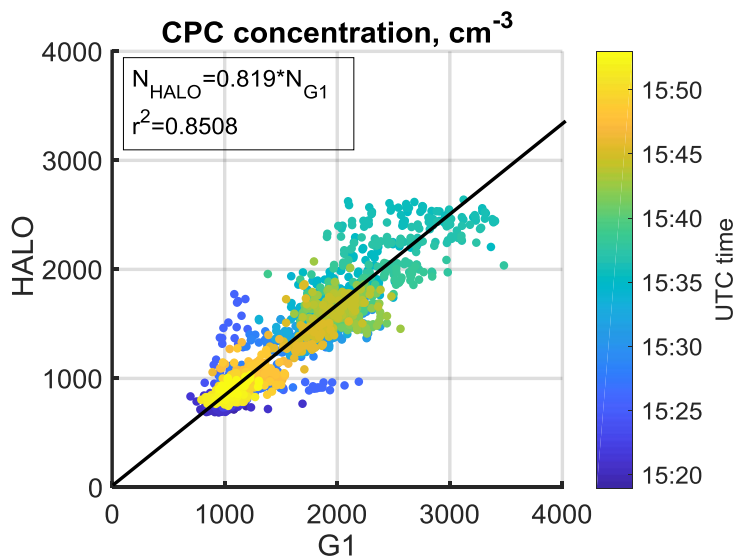
1136

1137   Figure 6. The G1 and HALO comparison for aerosol number concentration measured by CPC

1138   (>10 nm) on September 9.
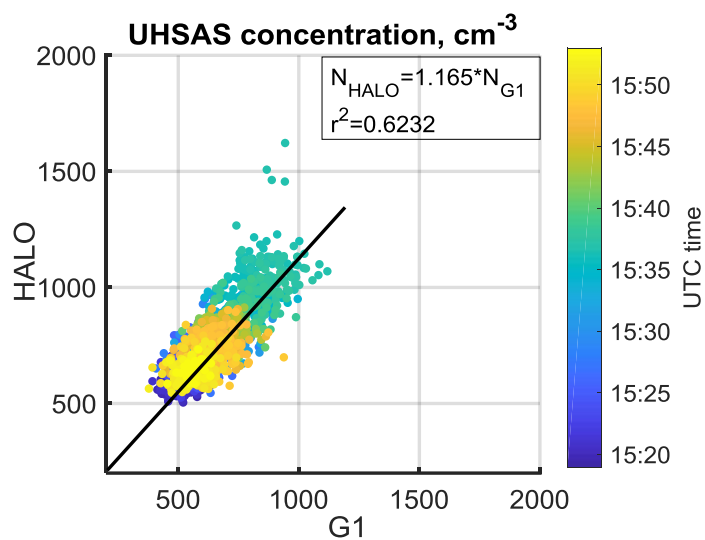
1139

Figure 7. The G1 and HALO comparison for aerosol number concentration measured by UHSAS (90-500 nm) on September 9.

1140

1141

1142

1143   (a)   (b)
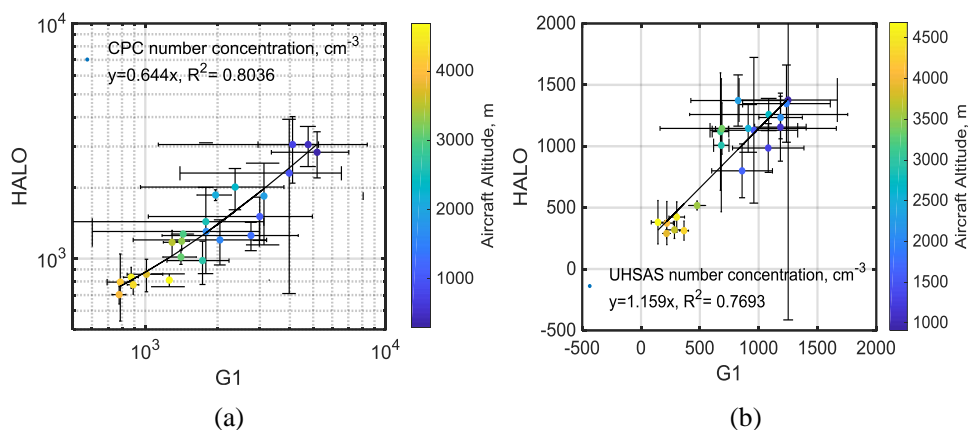
1144   **Figure 8.** The G1 and HALO comparison for aerosol number concentration profiling measured

1145   by (a) CPC and (b) UHSAS (100-700 nm) on September 21.
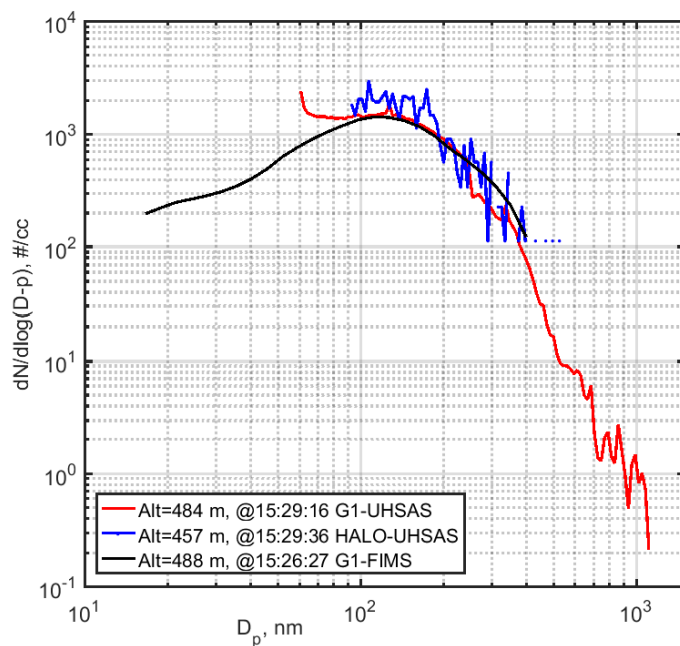
1146

Figure 9. The G1 and HALO comparison for aerosol size distribution measured by UHSAS

(from both aircraft) and FIMS (on the G1) on September 9.

1148

1149

Atmospheric
Measurement
Techniques
Discussions

1150

(a)   (b)   (c)   (d)
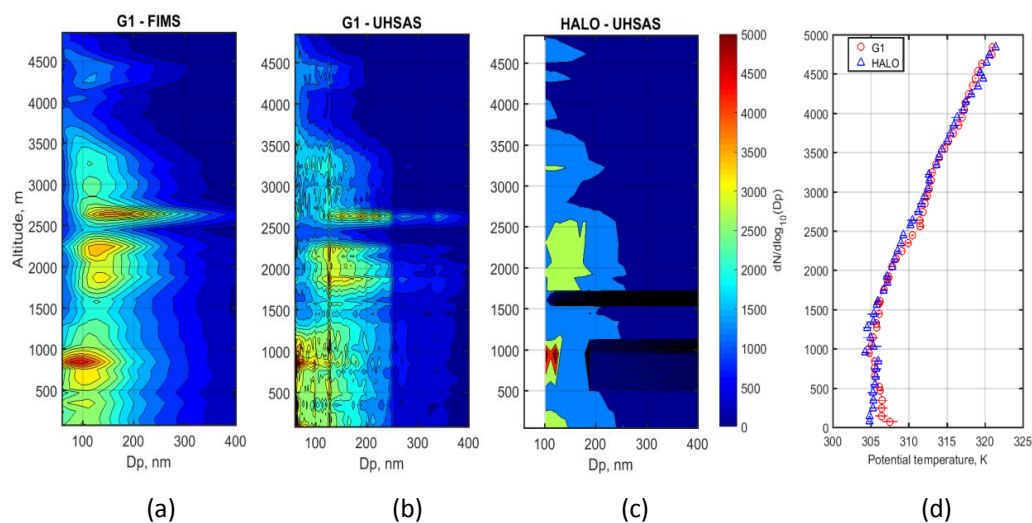
1151

1152   Figure 10. Aerosol size distribution vertical profiles measured by (a) the G1 FIMS, (b) The G1

1153   UHSAS, (c) the HALO UHSAS, (d) Potential temperature aboard the G1 and HALO on September

1154   21.

1155

1156   (a)   (b)
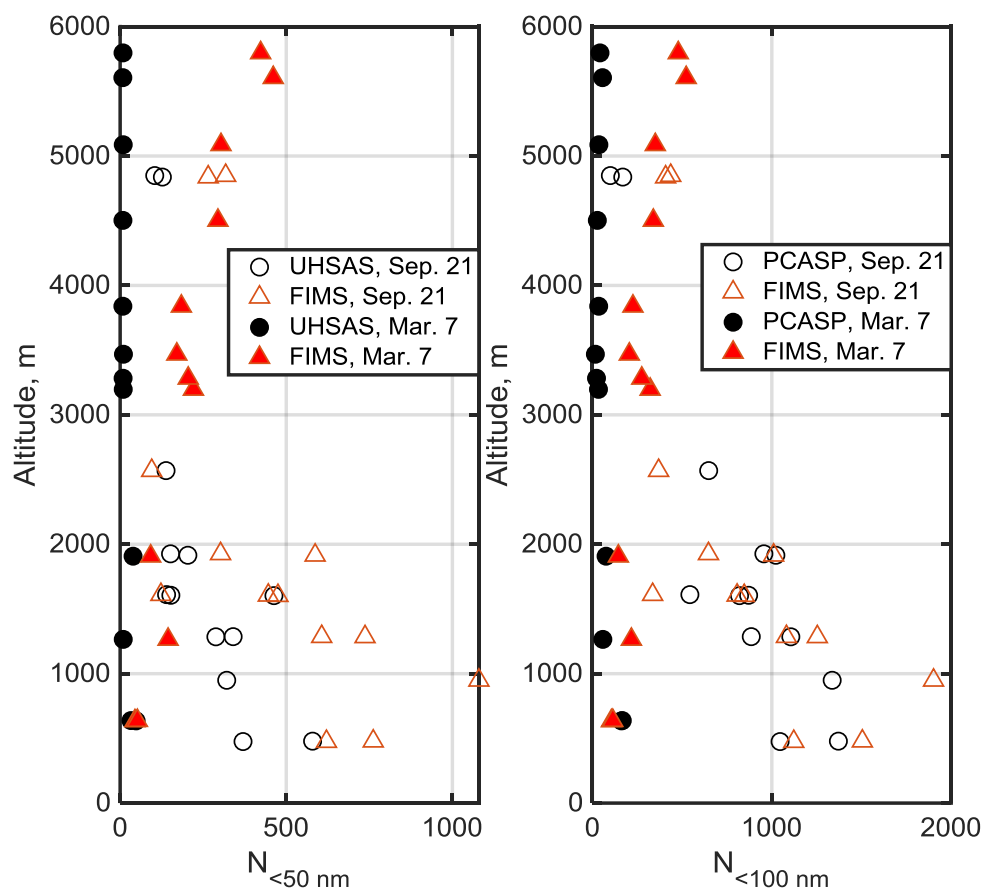
1157   Figure 11. Comparison of the number concentration for (a) sizes less than 50 nm and (b) sizes

1158   less than 100 nm. FIMS-measured size distribution and UHSAS/PCASP estimated size

1159   distribution are used.
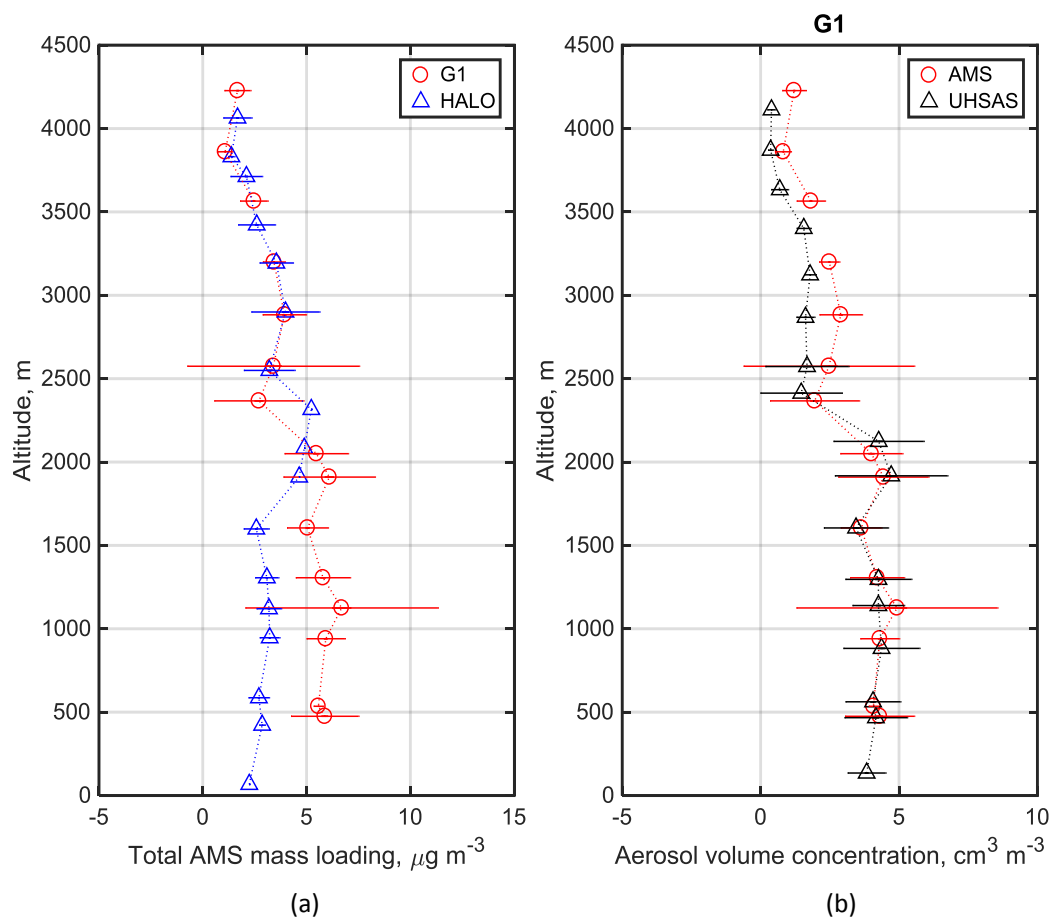
Figure 12. (a) Comparison of aerosol mass loading measured by the G1 and HALO AMS on September 21; (b) aerosol volume concentration comparison from AMS and the integrated UHSAS on the G1.
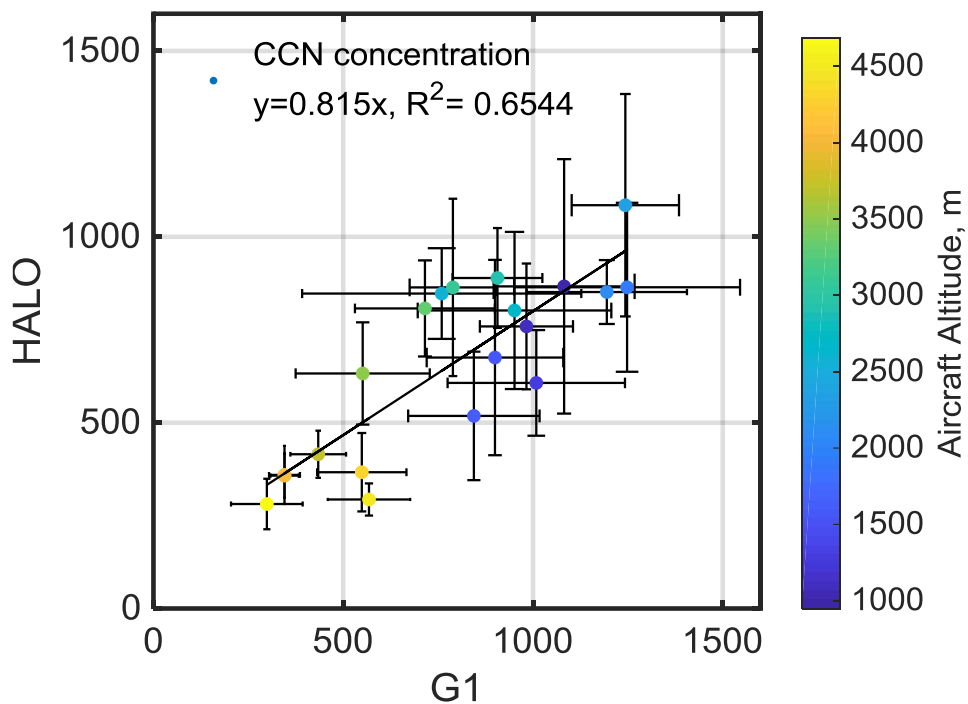
1165

Figure 13. The G1 and HALO comparison of aerosol CCN concentration (S=0.5%) measured
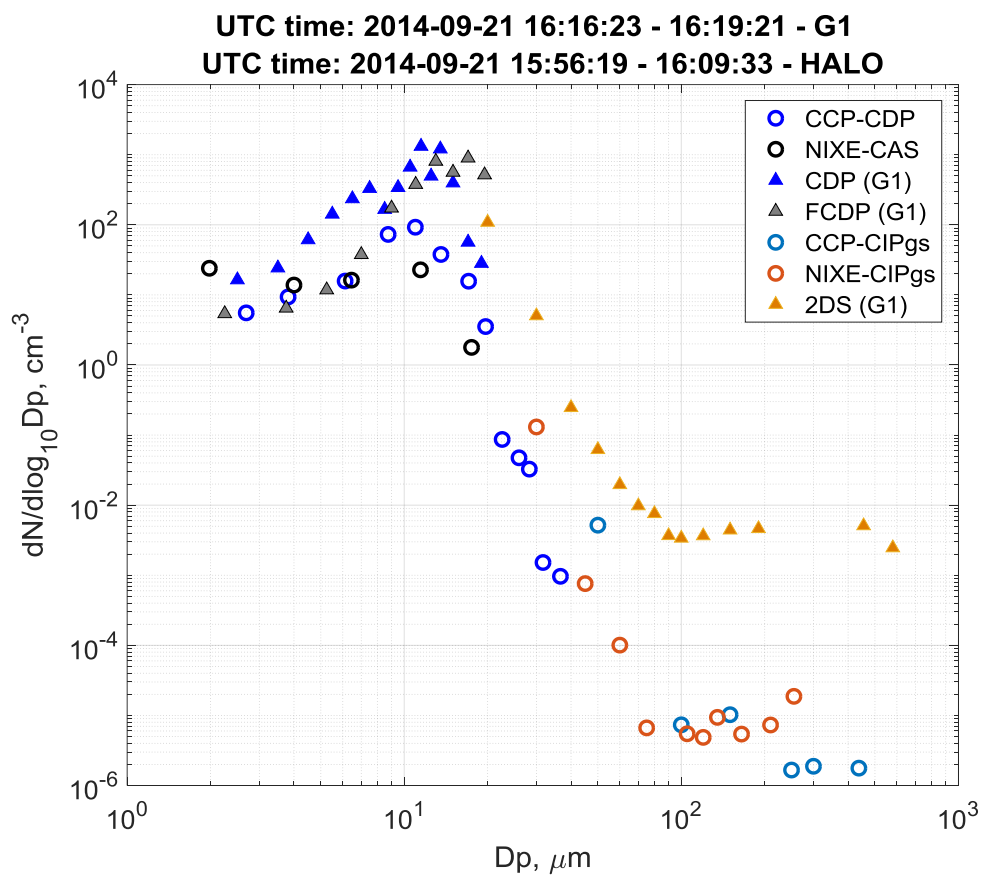on September 21.

1166

1167
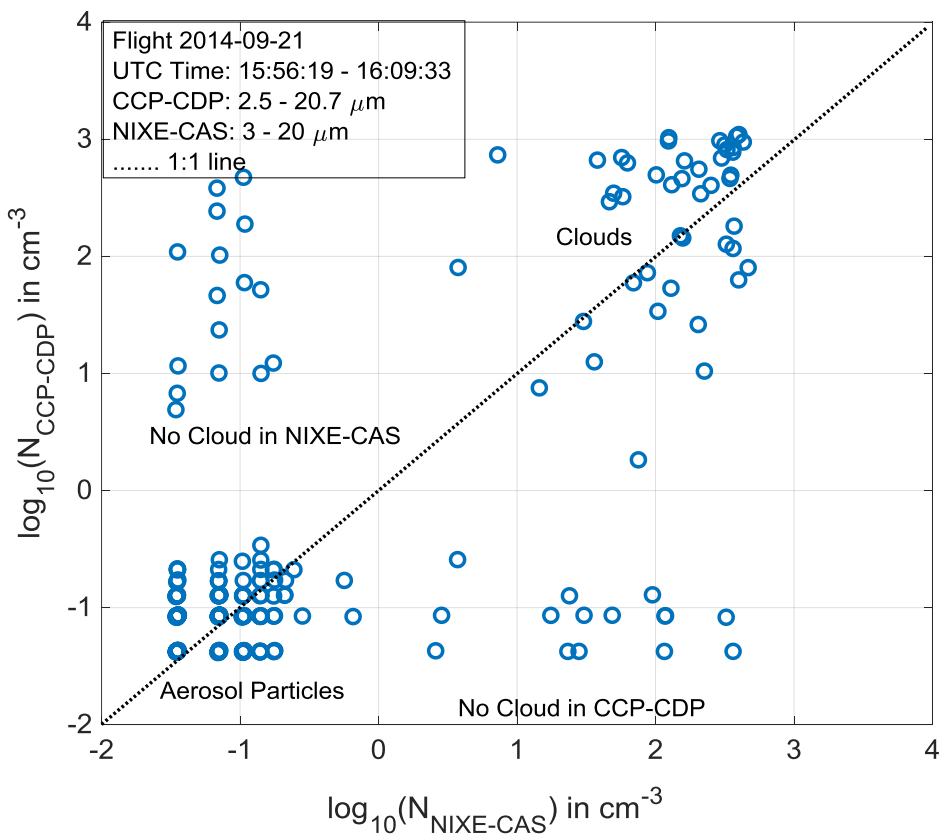
1168

1169   (a)
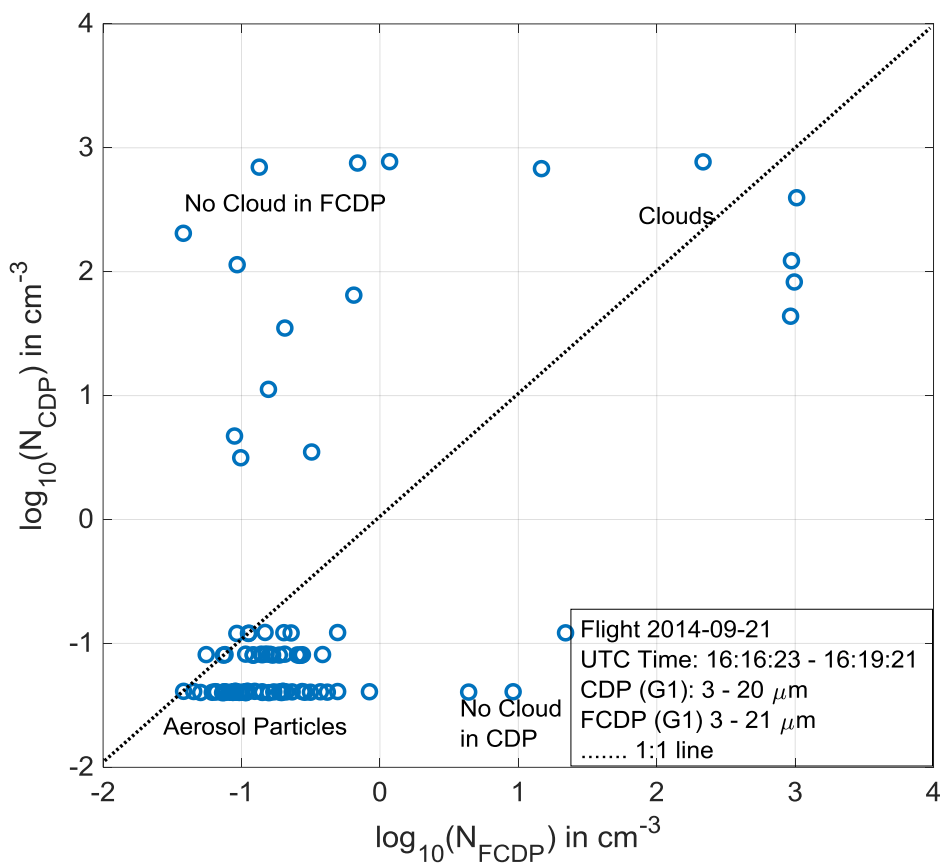
1170

1171   (b)

1172   Figure 14 The comparison of cloud droplet concentrations in the same aircraft (a) between
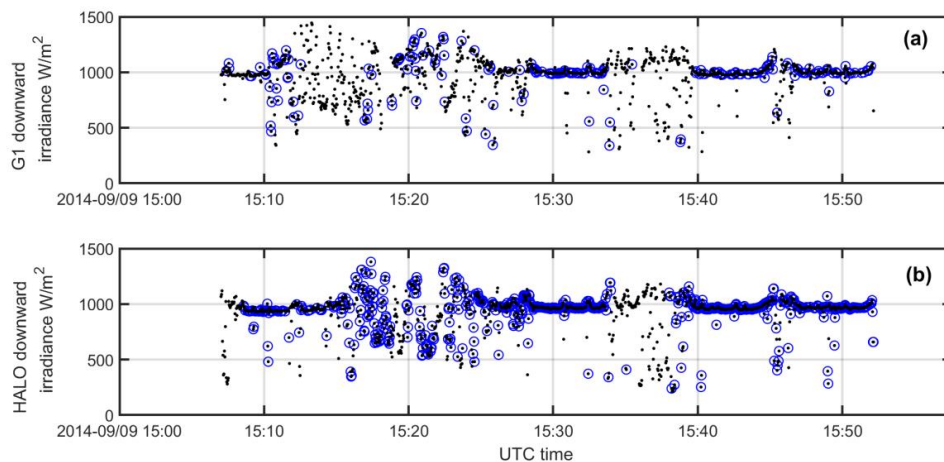
1173   NIXE-CAS and CCP-CDP on board HALO; (b) between CDP and FCDP on board the G1.
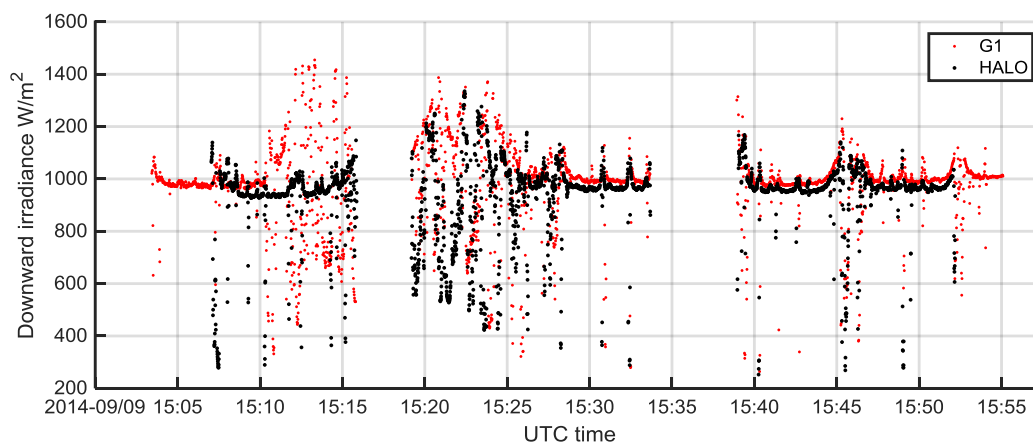
1174

1175   Figure 15. The cloud droplet size distribution from the cloud probes on the G1 and HALO.

1176

Figure 16. Time series of the G1 and HALO downward irradiance on September 9. The (a) by SPN-1 and (b) by SMART-Albedometer. Black dots represent all data under the general inter-comparison criteria. The blue circles represent the restricted navigation criteria.

Figure 17. Time series comparison of the G1 (SPN-1) and HALO (SMART-Albedometer) radiation measurements on September 9.

53